https://doi.org/10.5194/egusphere-2026-4393
Preprint. Discussion started: 17 August 2026

Contrasting air pollution and surface temperature trends in South and East Asia: satellite observations and CMIP6 simulations assessment

Selviga Sinnathamby[1], Sarah Safieddine[1], Anne Boynard[1,2], Juliette Hadji-Lazaro[1], Solène Turquety[1], Simon Whitburn[3,4], Lieven Clarisse[3], Marie Doutriaux-Boucher[5], Pierre Coheur[3] and Cathy Clerbaux[1,3]

[1] LATMOS/IPSL, Sorbonne Université, UVSQ, CNRS, Paris, France (selviga.sinnathamby@latmos.ipsl.fr)
[2] SPASCIA, Ramonville-Saint-Agne, France
[3] Spectroscopy, Quantum Chemistry and Atmospheric Remote Sensing (SQUARES), Brussels Laboratory of the Universe (BLU-ULB), Université libre de Bruxelles (ULB), Brussels, Belgium
[4] Royal Meteorological Institute of Belgium (KMI-IRM), Atmospheric Composition, Measurements and Modelling division (ACM²), Brussels, Belgium
[5] EUMETSAT, EUMETSAT Allee 1, D-64295, Darmstadt, Germany

Correspondence to: Selviga Sinnathamby (selviga.sinnathamby@latmos.ipsl.fr)

Abstract.

South and East Asia have experienced contrasting air pollution trends over recent decades, with implications for regional climate, particularly surface temperature. However, the consistency between recent satellite-observed changes and climate model projections remains under-documented. Using IASI, OMI, MODIS and CERES satellite observations, we examine how changes in gaseous pollutants (CO, NO_2, SO_2) and aerosol loading (AOD) are associated with surface temperature (T_{skin}) changes over South and East Asia during 2008-2025, considering other key variables affecting T_{skin} (cloud fraction, surface shortwave radiation ($SSW_{\downarrow}$), vegetation cover). We compare observed changes with CMIP6 simulations under SSP1-2.6, SSP2-4.5, and SSP3-7.0 and discuss their evolution up to 2100. Observations reveal strong declines in CO, NO_2, SO_2, and AOD over East Asia and increases over South Asia. These trends align with a strong warming over East Asia and daytime cooling over South Asia, consistent with cloud fraction and SSW↓ trends. Vegetation greening reinforces cooling in South Asia while being outweighed by increased SSW↓ in East Asia. CMIP6 simulations reproduce observed gaseous pollutant changes over East Asia most consistently with SSP1-2.6, whereas South Asia lies between SSP1-2.6 and SSP2-4.5. AOD in both regions falls between SSP1-2.6 and SSP2-4.5. However, CMIP6 models do not reproduce the observed regional contrast in surface temperature. The extended historical period in CMIP7, overlapping with the satellite era, will provide new opportunities to evaluate model representations of recent air pollution changes and their associated climate responses.

1. Introduction

Asia has experienced remarkable demographic, economic, and industrial growth at varying paces since the 1980s, most notably South Asia and East Asia. While this transformation has profoundly reshaped the continent within a few decades, it has also

https://doi.org/10.5194/egusphere-2026-4393
Preprint. Discussion started: 17 August 2026

been accompanied by a marked deterioration in air quality, driven by increasing anthropogenic emissions (Kurokawa and Ohara, 2020; Lelieveld et al., 2001; Turnock et al., 2020).

These emissions release a wide range of gaseous pollutants into the troposphere, such as carbon monoxide (CO), nitrogen oxides (NO_x) and sulfur dioxide (SO_2), as well as aerosols. CO is a toxic gas produced during incomplete combustion processes but also through oxidation reactions of methane and non-methane hydrocarbons (Seinfeld and Pandis, 2016). With its relatively long lifetime (few days to two months (Holloway et al., 2000)), CO can be transported over long distances and is therefore commonly used as a tracer of atmospheric pollution and biomass burning. NO_x, which include nitrogen oxide (NO) and nitrogen dioxide (NO_2), are emitted during fossil fuel combustion from sources such as vehicles, power plants, industries and biomass burning but also from natural sources (lightning, soil microbial processes). NO_x are highly reactive and short-lived in the boundary layer, with a lifetime of only a few hours (Lange et al., 2022) and most atmospheric NO_2 results from the rapid oxidation of NO (Seinfeld and Pandis, 2016). Besides volcanic sources, SO_2 is emitted primarily from the combustion of fossil fuels such as coal and oil, as well as from industrial activities including power generation, oil refining, and metal smelting. It is also highly reactive, with a lifetime ranging from a few hours to several days (Chen et al., 2025b; Lee et al., 2011). Aerosols are emitted by anthropogenic activities and natural processes (e.g., dust storms, sea spray, and volcanic eruptions) and can be formed through chemical reactions in the troposphere. SO_2 and NO_x are important aerosol precursors, as they undergo rapid chemical transformation into secondary inorganic aerosols, mainly sulfate and nitrate, through nucleation and condensation processes (Szopa et al., 2021). Although CO is not a direct aerosol precursor, it can serve as a proxy for primary carbonaceous aerosols, especially black carbon, since they are often co-emitted during incomplete combustion. The lifetime of aerosols is relatively short, ranging from a few hours to a few days, depending on their size and removal processes through dry and wet deposition (Jacob, 2000).

Exposure to gaseous pollutants and aerosols, in particular fine particulate matter (PM), is detrimental to human health, since they can induce cardiovascular and respiratory diseases, leading to increased morbidity and premature mortality (Chen et al., 2007; Cui et al., 2022; Jo et al., 2026). Beyond its health impact, air pollution also influences the Earth's climate by altering the atmospheric and surface energy budgets. Gases can directly modify the Earth's radiative balance through the absorption and emission of radiation or indirectly through atmospheric chemical processes leading to the formation of radiatively active species such as ozone and aerosols. The radiative impacts of aerosols depend on particle size, chemical composition and loading and occur through two main mechanisms (Forster et al., 2021) : aerosol-radiation interaction (ARI) and aerosol-cloud interactions (ACI). ARI refers to the direct effect via the scattering and absorption of shortwave radiation and is more directly related to aerosol loading and optical properties, commonly represented by the Aerosol Optical Depth (AOD). ACI is the indirect effect, where aerosols act as cloud condensation nuclei (CCN) and modify the radiative properties and lifetime of clouds (Albrecht, 1989; Twomey, 1974). Through these interactions, aerosols and clouds can substantially modify the amount of solar radiation reaching the surface, potentially contributing to regional surface cooling or warming depending on aerosol optical properties and atmospheric conditions (Huang et al., 2006; Krishnan and Ramanathan, 2002; Sarangi et al., 2018). While aerosols and clouds modulate incoming shortwave radiation, surface temperature also depends on the partitioning of

https://doi.org/10.5194/egusphere-2026-4393
Preprint. Discussion started: 17 August 2026

surface energy into radiative and turbulent fluxes which are modulated by surface characteristics such as albedo, roughness, and vegetation cover. In particular, vegetation affects surface temperature through changes in evapotranspiration and albedo, depending on the vegetation type and environmental conditions (Li et al., 2015; Yang et al., 2020, 2019).

Monitoring long-term variations in atmospheric pollution is thus essential to assess its potential impact on regional climate. However, air quality monitoring stations remain spatially limited and unevenly distributed across Asia. In South Asia in particular, long-term trend analysis is difficult because measurements are sparse, often shorter than a decade, and sometimes affected by data quality issues (Vohra et al., 2025). Satellite observations offer consistent monitoring of the Earth's atmosphere and surface at large spatial scales and relatively long time periods, making them well suited for investigating pollutant trends and their potential influence on climate variables.

Trend studies of CO, NO_2, SO_2, and AOD using satellite observations over Asia are well established (Buchholz et al., 2021; Fan et al., 2025; Rahman et al., 2023; Ul-Haq et al., 2015; Wang et al., 2018; Zhang et al., 2020). These studies have documented notable changes in air pollution over recent decades, reflecting the impact of emission control policies across the region. This is particularly true for China where strong air quality regulations, such as the Air Pollution Prevention and Control Action Plan (APPCAP) deployed in 2013, have led to significant declines in pollutant levels (De Leeuw et al., 2024; Peng et al., 2025; Tang et al., 2026). In India, although air quality policies have been implemented, such as the National Clean Air Programme (NCAP) introduced in 2019, their effectiveness in reducing emissions and improving air quality remains uncertain (Gulia et al., 2022; Guttikunda et al., 2025; Xie et al., 2024). In neighbouring countries, national air quality regulations are only now being introduced, such as Pakistan with the National Clean Air Policy in 2023, and Bangladesh with the National Air Quality Management Plan for 2024-2030 (Ministry of Environment, Forest, and Climate Change, 2024; Ministry of Climate Change, 2023).

The air pollution variability and regulations over the last decades have implications for the regional climate, through their influence on aerosol-cloud dynamics and consequently, surface temperature (Chen et al., 2025a; Kant et al., 2022; Sarin and Vinoj, 2026). Over the last decades, the availability of advanced satellite instruments has made it possible to monitor both atmospheric composition and temperature changes concurrently, but most studies have focused on either air pollution or temperature trends separately. To our knowledge, few studies have jointly examined air pollution and surface temperature trends in Asia over the last two decades (2008-2025), based on long-term satellite observations. Furthermore, while future aerosol and temperature trends are frequently discussed, the future evolution of gaseous pollutants remains under documented, despite many of these species acting as essential aerosol precursors (Pathak and Kuttippurath, 2026; Ramachandran et al., 2022; Ren et al., 2024; Samset et al., 2019). In particular, there is a gap in the literature on the extent to which current observations (of air pollutants and surface temperature) compare with the future projections defined within the sixth phase of the Coupled Model Intercomparison Project (CMIP6) scenarios, which were used in the last Intergovernmental Panel on Climate Change assessment report (IPCC, 2023).

Here, we investigate the evolution of air pollution in South and East Asia alongside changes in surface temperature over the recent decades (2008-2025) and through the end of the century (2008-2100). To do so, we combine observations from a diverse

https://doi.org/10.5194/egusphere-2026-4393
Preprint. Discussion started: 17 August 2026

suite of polar-orbiting satellite instruments, including the Infrared Atmospheric Sounding Interferometer (IASI, Clerbaux et al., 2009), the Ozone Monitoring Instrument (OMI, Levelt et al., 2006), the Moderate-Resolution Imaging Spectroradiometer (MODIS, Xiong & Barnes, 2006), and the Clouds and the Earth's Radiant Energy System (CERES, Wielicki et al., 1996), with simulations from selected CMIP6 models under various future scenarios (Sect. 2). We first analyze the drivers of observed regional surface temperature trends to identify their underlying mechanisms in Sect. 3. This includes an assessment of air pollutants (both aerosols through AOD and gaseous species such as CO, NO_2 and SO_2), cloud fraction, incoming shortwave radiation (Surface Shortwave Downward Flux, $SSW_{\downarrow}$) and vegetation cover, represented by the Normalized Difference Vegetation Index (NDVI). We then assess how regional air pollution and surface temperature changes align with different CMIP6 Shared Socio-economic Pathways (SSP) over the 2008-2025 period, evaluating the extent to which current observational trends are captured by model projections (Sect. 4). The future evolution of air pollutants and their implications for future surface temperature trends are examined in Sect. 5, followed by a discussion and conclusion.

2. Datasets and methods

2.1. Satellite observations

2.1.1. CO concentrations, cloud fraction and skin temperature from IASI

In this study, we use three IASI Level-2 data products: CO total columns, cloud fraction, and skin temperature (T_{skin}). IASI is a nadir-viewing Fourier Transform Spectrometer that has been measuring the Earth-atmosphere system's thermal infrared emission in the 645-2760 cm^{-1} spectral range since 2007, aboard the polar-orbiting meteorological satellites Metop-A, -B and -C. With a swath width of 2200 km, IASI achieves global coverage twice a day at 09:30 a.m./p.m. local solar time. Each IASI field of view is composed of four pixels with a 12 km diameter circular footprint at nadir, expanding to a 20×39 km elliptical footprint at the swath extremities. A wide range of meteorological parameters and columnar concentrations of diverse trace gases can be retrieved from IASI radiances, thanks to its excellent spectral resolution of 0.5 cm^{-1} (apodised) and low radiometric noise (Clerbaux et al., 2009). Metop-A has been in drifting orbit since mid-2019 and Metop-B since late 2022. Although Metop-A was officially decommissioned in October 2021, the IASI mission has provided over 19 years of continuous data and is expected to last until at least 2030 with Metop-C. This extensive dataset enables long-term global atmospheric monitoring, from tracking pollution from anthropogenic sources (Boynard et al., 2014; Clarisse et al., 2011) and biomass burning (Ehret et al., 2025; Sinnathamby et al., 2026; Turquety et al., 2009) to evaluating thermal comfort in the context of climate change (Safieddine et al., 2022). Beyond atmospheric composition and surface applications, IASI measurements have also been used to estimate spectrally resolved outgoing longwave radiation and investigate radiative forcing (Whitburn et al., 2021, 2026).

CO total columns

IASI CO total columns are obtained from the Climate Data Record (CDR, AC SAF, 2024a) and near-real time (NRT) products. Both datasets are generated using the same version of the Fast Optimal Retrievals on Layers for IASI (FORLI) v20151001 algorithm (George et al., 2015; Hurtmans et al., 2012), ensuring consistency across the time series. The CDR is based on reprocessed IASI Level 1C radiances and meteorological input fields and spans from July 2007 to December 2023 for Metop-A and Metop-B (EUMETSAT, 2025). IASI CO retrievals show maximum sensitivity around 5-7 km, while near-surface sensitivity is strongly dependent on the thermal contrast (Bauduin et al., 2017; Clerbaux et al., 2009). We only consider daytime observations (solar zenith angle < 90°) and the most reliable pixels (general quality flag of 2 and cloud cover <25%).

Cloud fraction

Cloud fraction is obtained from the IASI Cloud Detection product, which is derived from a supervised neural network developed by Whitburn et al. (2022). This algorithm uses IASI radiances selected outside the spectral regions sensitive to CO_2 and water vapor, ensuring the dataset's stability over time and hence suitability for climate studies. The Cloud Detection product has been evaluated against the operational IASI Level 2 cloud product and other satellite-based cloud datasets, showing good agreement and consistent performance over the IASI time series (Whitburn et al., 2022). We only consider daytime observations (solar zenith angle < 90°).

Skin temperature (T_{skin})

T_{skin} is obtained from the latest version of the clear-sky IASI skin (surface) temperature neural network product (Safieddine et al., 2020, 2026). The IASI T_{skin} product has been evaluated through a global comparison with other satellite products and reanalysis data, showing broadly consistent spatial patterns and temporal variability over the 2008-2022 period (Safieddine et al., 2026).

IASI data processing

For each L2 product, we combine observations from the three Metop platforms to ensure a continuous 18-year time series, as follows:

- January 2008 - February 2013: Metop-A only
- March 2013 - December 2019: Metop-A and Metop-B combined
- January 2020 - December 2025: Metop-B and Metop-C combined

Metop-A is excluded after 2019 due to its orbital drift. Regarding T_{skin}, only Metop-C is considered after 2023, to avoid biases on local overpass times introduced by the orbital drift of Metop-B. For all IASI datasets, monthly grids were obtained by averaging 1°×1° daily grids, generated from the Level 2 data described above.

2.1.2. Tropospheric NO_2 and SO_2 concentrations from OMI

We use here tropospheric NO_2 and SO_2 concentrations from OMI aboard NASA's Aura satellite, operational since 2004. OMI measures solar backscattered radiation in the ultraviolet and visible range (260-500 nm) at a local overpass time at 01:45 p.m. Its spatial resolution extends from approximately 13×24 km² at nadir, to 24×160 km² at swath edges with a global coverage of approximately every two days (Lamsal et al., 2021). OMI provides the only continuous and consistently reprocessed satellite record of both tropospheric NO_2 and SO_2 over the 2008-2025 period, making it particularly well suited for long-term trends globally, including Asia (Ali et al., 2024; Krotkov et al., 2016; Li et al., 2017; Rahman et al., 2023).

Tropospheric NO_2 vertical column densities

Tropospheric NO_2 vertical column densities (VCDs) are obtained from the Level 2 OMI NO_2 standard product, version 5 (OMNO2) (Krotkov et al., 2024a). The retrieval is performed in the 402-465 nm spectral range using Collection 4 Level 1B data. The algorithm employs a spectral fitting technique to estimate slant column densities which are subsequently converted to VCDs using Air Mass Factors (AMFs) (Bucsela et al., 2013). Only good quality pixels are selected here, i.e. with a cloud fraction < 30%, solar zenith angle < 85° and a "XTrackQualityFlagsModified" value of 0 (Krotkov et al., 2024b).

SO_2 vertical column densities

SO_2 VCDs are obtained from the Level 2 SO_2 standard product, version 2.1 (OMSO2) (Krotkov and Li, 2025). The retrieval algorithm uses an updated principal component analysis (PCA)-based algorithm in the 310-340 nm range to derive SO_2 SCDs, which are converted to VCDs using pixel-specific SO_2 Jacobian (AMFs) and updated monthly model-based a priori profiles. High-quality observations are used here, i.e., scenes near the center of the swath (rows 4-54), with solar zenith angle < 65°, cloud radiance fraction < 0.3 and AMF > 0.3 (Krotkov and Can, 2025).

OMI retrieval sensitivity and data processing

Both NO_2 and SO_2 retrievals rely on the conversion of slant column densities into VCDs using AMFs. AMFs characterize the vertical sensitivity of the retrieval and depend on observation conditions, including cloud and aerosol loading. Sensitivity to near-surface trace gases is generally reduced, particularly under high cloud or aerosol conditions (Boersma et al., 2004; Lamsal et al., 2021; Li et al., 2020).

For this study, NO_2 and SO_2 data are gridded at a 1°×1° spatial resolution from the Level 2 products. For SO_2, we apply a Hampel filter to the daily grids to reduce the impact of volcanic SO_2 plumes on the monthly averages (Hampel, 1974).

2.1.3. AOD and NDVI from MODIS

We use here MODIS observations to characterize both aerosols loading and vegetation cover changes through Aerosol Optical Depth (AOD) and Normalized Difference Vegetation Index (NDVI), respectively. MODIS observes radiation reflected and emitted by the Earth and its atmosphere in the visible and infrared ranges (0.4-14.4 µm) along a 2300 km-wide swath (Xiong and Barnes, 2006). It has been operating on the Terra satellite since 2000 and crosses the equator at approximately 10:30 a.m./p.m. local time, with a revisit time of 1-2 days.

Aerosol Optical Depth (AOD)

AOD at 550 nm from MODIS Terra is used in this study to quantify the light extinction by aerosols. We specifically use daily 1°×1° grids from the Level 3 MOD08D3 product (MODIS Atmosphere Science Team, 2015), derived from the Level 2 MOD04 product at a spatial resolution of 10km. MODIS AOD products have been validated in East and South Asia against aircraft, AERONET and other satellite measurements (Choi et al., 2019; Payra et al., 2023; Su et al., 2022; Wei et al., 2019), showing good performance in representing regional aerosol loading. The Level 2 AOD retrieval uncertainty over land is

https://doi.org/10.5194/egusphere-2026-4393
Preprint. Discussion started: 17 August 2026

estimated to be ±(0.05 + 0.15 × AOD) for the Dark Target retrieval and ±(0.03 + 0.20 × AOD) for the Deep Blue retrieval**.** Monthly grids were obtained by averaging the MOD08D3 daily grids.

Normalized Difference Vegetation Index (NDVI)

To characterize land surface changes, particularly to assess the extent to which vegetation cover influences surface temperature trends, we use the NDVI also from MODIS Terra, more specifically the monthly MOD13A3 Version 6.1 product (Didan, 2021). This dataset is given at 1km spatial resolution and was gridded at a spatial resolution of 1°×1°. NDVI represents vegetation greenness and density and is calculated from reflectance in the red (0.6 -0.7 µm) and near-infrared (NIR, 0.7-1.1 µm) bands, as:

$$NDVI = \frac{NIR - Red}{NIR + Red} \quad (1)$$

NDVI values range from −1 to 1 with low values (< 0.2) indicating bare surfaces (urban areas or sparse vegetation) and high values (> 0.5) dense vegetation cover (tropical forests).

2.1.4. Surface Shortwave Downward Flux ($SSW_\downarrow$) from CERES

As T_{skin} depends on the amount of solar radiation reaching the surface, we use Surface Shortwave Downward Flux ($SSW_\downarrow$) from CERES to examine how atmospheric processes modulate surface radiation and consequently T_{skin} trends. The CERES instruments, which are currently operating on the Terra, Aqua, Suomi-NPP and NOAA-20 satellites, measure broadband radiances across the 0.3-200 µm spectral region, including the shortwave region (0.3-5 µm). These observations are used to derive top-of-atmosphere (TOA) and surface radiative fluxes (irradiances) at spatial resolutions ranging from 20 to 24 km, depending on the satellite.

We use here 1×1° monthly grids of $SSW_\downarrow$ given by the Energy Balanced and Filled (EBAF) Edition 4.2.1. dataset, as it is the only consistent satellite-based product over the 2008-2025 period (Kato et al., 2018, 2025; Loeb et al., 2018). This product estimates all-sky and clear-sky $SSW_\downarrow$ through radiative transfer calculations using cloud and aerosols properties from MODIS and VIIRS along with temperature and humidity profiles from MERRA-2 reanalysis. These fluxes are constrained by CERES TOA irradiances from Terra and Aqua through March 2022 and NOAA-20 thereafter (Loeb et al., 2024). Comparison with surface observations indicate an uncertainty of approximately 12 W/m² for the EBAF surface shortwave irradiance over land (Kato et al., 2018). Both clear-sky and all-sky $SSW_\downarrow$ are discussed in this study.

2.2. MERRA-2 reanalysis

Air temperature at 2 meters (T_{2m}) and clear-sky $SSW_\downarrow$ from the Modern-Era Retrospective analysis for Research and Applications Version 2 (MERRA-2, Gelaro et al., 2017) reanalysis are used in this study to link the observed IASI T_{skin} trends with atmospheric processes, specifically at IASI overpass times. MERRA-2 is produced by NASA Global Modeling and Assimilation Office (GMAO) using the Goddard Earth Observing System Model (GEOS) version 5.12.4. It incorporates and assimilates a wide range of observations, including satellite observation of AOD from MODIS making it suitable for our study.

https://doi.org/10.5194/egusphere-2026-4393
Preprint. Discussion started: 17 August 2026

T_{2m} and clear-sky $SSW_{\downarrow}$ are retrieved from the M2T1NXSLV and M2T1NXRAD collections, respectively. These datasets are given at a spatial resolution of 0.5°×0.625° and a temporal resolution of 1-hour, and are matched to IASI overpasses in both time and space. The collocated data are then regridded onto a 1×1° grid.

2.3. Anthropogenic emissions from CAMS-GLOB-ANT and fire emissions from GFAS

To assess changes in anthropogenic and fire emissions over 2008-2025, we used the CAMS-GLOB-ANT and the Global Fire Assimilation System (GFAS) emission inventories. The CAMS-GLOB-ANT version 6.2 provides the yearly emissions of pollutants in different sectors such as CO, SO_2 and NO_x (Soulie et al., 2024). The methodology consists of using the Community Emissions Data System (CEDS) emissions to extrapolate emissions the Emissions Database for Global Atmospheric Research (EDGAR) version 6 and 7 up to 2026 (Crippa et al., 2018, 2021). For China, extrapolation was instead performed using REAS trends (2012-2015) for available species and sectors to ensure better regional agreement (Denier van der Gon et al., 2025). Fire emissions of CO and NO_x are derived from GFAS, which estimates daily fire fluxes by assimilating fire radiative power from satellite observations (Kaiser et al., 2012). We use here a combination of the versions 1.2 (January 2008- November 2025), based on MODIS Aqua and Terra data, and 1.4 (December 2025), which incorporates VIIRS Suomi-NPP observations in supplement.

2.4. CMIP6 simulations

2.4.1. Model and scenario selection

To examine the present and future evolution of pollutants and surface temperature, we work with outputs from selected Earth system models contributing to CMIP6 (Eyring et al., 2016), as detailed in Table 1. Among all the models contributing to CMIP6, only three currently provide all the required outputs for our study (CO, NO_2 (including tropopause height), SO_2, AOD at 550 nm, and surface temperature) across both the historical simulation (2008-2014) and the SSP1-2.6, SSP2-4.5, and SSP3-7.0 future scenarios (2015-2100). We chose these scenarios to capture a full range of future evolutions of air pollution and surface temperature. They span from a low-warming pathway with SSP1-2.6, where global radiative forcing reaches 2.6 W/m^2 by the end of the century, to a high-warming pathway with SSP3-7.0, reaching 7.0 W/m^2. Between these two pathways, SSP2-4.5 represents a "middle-of-the-road" pathway that follows historical trends, with a moderate radiative forcing reaching 4.5 W/m^2 by 2100 (O'Neill et al., 2016). Air quality trajectories in SSPs are defined by the stringency of pollution control measures and the timing of their implementation at the global and regional scales, but also on the co-benefits arising from climate mitigation policies (Rao et al., 2017; Riahi et al., 2017). While the SSP1-2.6 combines strong climate mitigation, such as transition to cleaner energies and decarbonized transport and industries, with strict pollutant emissions control, SSP3-7.0 represents the opposite extreme. In SSP3-7.0, a lack of climate mitigation policies and delayed air quality regulations in developing countries lead to less efficient emission control than in SSP1-2.6. This scenario also features high population growth and economic development fuelled by fossil fuels, with an increasing contribution of coal to the energy mix at the end

https://doi.org/10.5194/egusphere-2026-4393
Preprint. Discussion started: 17 August 2026

of the century. Meanwhile, SSP2-4.5 follows a similar pathway to SSP1-2.6 but adopts a more gradual and less ambitious approach to pollution control. Here, only a single simulation (variant) is considered for each model. The corresponding variant labels are given in Table 1.

Model/Institution	Horizontal and vertical resolution	Variant	Model references	Data citation
GFDL-ESM4/NOAA	1.25°×1° 49 levels (top level 0.01 hPa)	r1i1p1f1	Dunne et al., 2020 Horowitz et al., 2020	John et al., 2018; Krasting et al., 2018
MRI-ESM2-0/MRI	1.125° × 1.125° (surface temperature, AOD) 2.8125° × 2.8125° (CO, NO_2, SO_2) 80 levels (top level 0.01 hPa)	r1i1p1f1	Yukimoto et al., 2019 Oshima et al., 2020	(Yukimoto et al., 2019b, a)
UKESM1-0-LL/MOHC	1.875×1.25° 85 levels (top level 85 km)	r1i1p1f2	Sellar et al., 2019 Archibald et al., 2020; Mulcahy et al., 2018	Good et al., 2019; Tang et al., 2019

Table 1. Description of CMIP6 models used in this study.

Anthropogenic and biomass burning emissions from the Community Emissions Data System (CEDS, Hoesly et al., 2018) and BB4CMIP (Van Marle et al., 2017) datasets, respectively, which were both developed in support of CMIP6, are used as input emissions. Note that the BB4CMIP dataset for the era since 1997 is built upon the Global Fire Emissions Database (GFED4.1s, van der Werf et al., 2017), which is directly derived from satellite observations of fire activity (e.g., burned areas and thermal anomalies from MODIS). While anthropogenic and biomass-burning emissions are prescribed, other natural emissions (e.g., dust and biogenic volatile organic compounds) are calculated internally and depend on the configuration of each model (see references in Table 1 for detailed information).

2.4.2. Processing CMIP6 outputs for comparison with satellite observations

All outputs from selected models are re-gridded to the same spatial resolution of the coarsest model (3×3°) then averaged to produce the multi-model mean. For the gaseous pollutants, vertical profiles are converted beforehand to column concentrations in order to compare with the satellite products. CO and SO_2 total column are calculated by integrating over pressure levels, from the surface to the top level as defined in the model configuration. Tropospheric NO_2 column is calculated by integrating from the surface to the tropopause height, which is also given by the same simulations. We decided to not smooth the model profiles with the satellite instruments' averaging kernels (AK), contrary to standard practice (Pandey et al., 2025). The AKs, which represent the vertical resolution and sensitivity of the retrieval, vary significantly with instantaneous atmospheric conditions, such as thermal contrast for thermal infrared sounders (Bauduin et al., 2017). As CMIP6 outputs are provided as monthly averages, applying monthly averaged AKs would be physically inconsistent. Averaging AKs over a month erases the key information needed to properly represent the instrument's vertical resolution, leading to a loss of physical representativeness.

2.5. Linear trend estimation and regions of study

Trend analysis for each variable is performed using quantile regression at the median (Koenker and Bassett, 1978) on monthly data, which were beforehand deseasonalized by subtracting the monthly climatology (average over the 2008-2025 period) from the original data. To account for temporal autocorrelation and non-normal error distributions, trends standard error and significance are estimated using the moving block bootstrap (MBB) method (Fitzenberger, 1998). The MBB approach consists of resampling overlapping blocks of the time series to generate synthetic series of the same length, from which linear slopes (trend values) are estimated. Trend standard error is defined as the standard deviation of the bootstrap linear slopes. Trends are considered statistically significant at the 95% confidence level (2σ) and their values are expressed in percent per decade (%/dec) after normalization by the 2008-2025 average, except for surface temperature trends which are reported in °C/dec. Regional analysis is made over the AR6 reference regions East Asia (EAS) and South Asia (SAS) as defined in Iturbide et al (2020), but restricted to land areas below 2 km elevation to exclude high-altitude regions such as the Himalayas. Regional means and trends discussed in Sect. 3, as well as relative changes in Sect. 4 and 5, are therefore representative of the low-elevation regions where most pollution sources and population are located. The SAS region extends from southern Pakistan, India, Bangladesh to Myanmar, while East Asia encompasses mainly Eastern China, the Korean Peninsula and Japan. An elevation map including the cities and sub-regions discussed in Sect. 3 is provided in the Supplement (Fig. S1). Trend values discussed in Sect. 3 are calculated from the regional mean monthly anomaly time series for each reference region.

3. Observed trends in air pollutants and their impact on the regional climate (2008-2025)

3.1. Regional evolution of gaseous pollutants (CO, NO_2 and SO_2) and aerosol loading (AOD)

Figure 1 shows the average spatial distribution of CO, NO_2, SO_2 and AOD across Asia over the 2008-2025 period in panels a, c, e and g, respectively. Their corresponding annual trends are illustrated in panels b, d, f and h, where hatched areas denote statistical significance. Trends are calculated on a 1×1° grid and are only shown for grid cells with at least 70% data availability. Since relative trends are normalized by the mean concentration over the study period, they can become artificially large in regions with very low background concentrations. Therefore, to avoid spurious relative trends resulting from normalization by very small mean concentrations, values are only displayed for cells where the average concentration exceeds 0.5×10^{15} molecules/cm² for NO_2 and 0.01 DU for SO_2. Trends values with their associated standard errors for each variable across South and East Asia (represented by the magenta lines in panel a) are provided in Fig. 3.

https://doi.org/10.5194/egusphere-2026-4393
Preprint. Discussion started: 17 August 2026

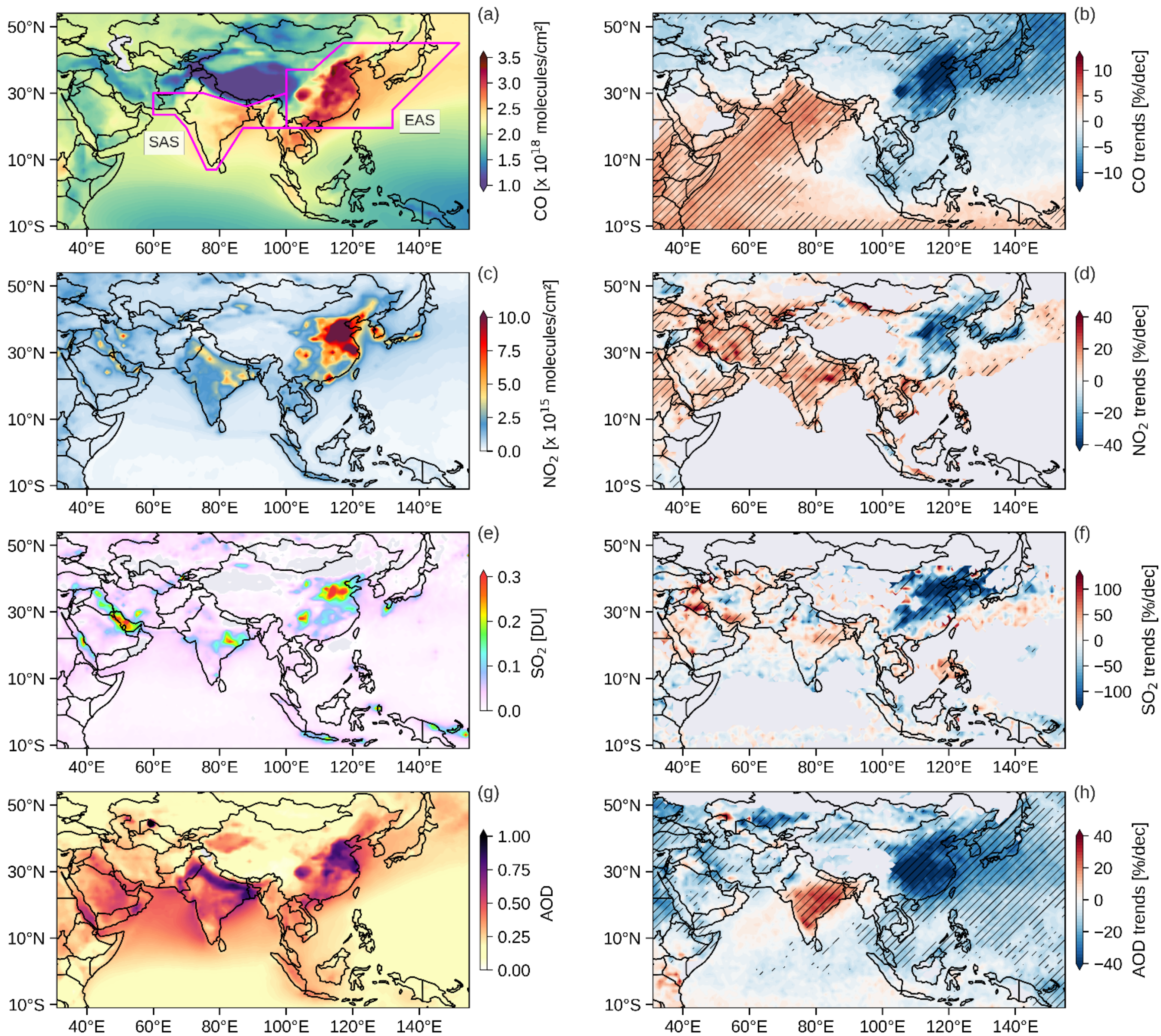

Figure 1. Left column (top to bottom): spatial distributions of CO (a), NO_2 (c) and SO_2 (e) concentrations, and AOD (g) averaged over the 2008-2025 period. Right column (top to bottom): corresponding trends at a 1×1° spatial resolution for CO (b), NO_2 (d), SO_2 (f) and AOD (h) over 2008-2025. Hatched areas indicate statistically significant trends. East Asia (EAS) and South Asia (SAS) are delimited by the solid lines in magenta on panel (a).

From Fig. 1a, 1c and 1e, we observe a distinct regional difference in average CO, NO_2 and SO_2 concentrations between South Asia and East Asia. For CO, East Asia exhibits a higher mean value (2.6×10^{18} molecules/cm²) and greater spatial variability than South Asia (2.3×10^{18} molecules/cm²). Within the East Asian region, the highest CO levels (> 3×10^{18} molecules/cm²) are

https://doi.org/10.5194/egusphere-2026-4393
Preprint. Discussion started: 17 August 2026

observed across Eastern China and the Sichuan Basin. In South Asia, the highest CO concentrations are found over the eastern part of India and Bangladesh (> 2.5×10^{18} molecules/cm²), particularly along the eastern Indo-Gangetic Plain (IGP).

NO_2 and SO_2 share very similar spatial patterns, as both gases are short-lived and share some common anthropogenic sources and so, remain concentrated close to emission sources. The highest NO_2 concentrations (> 4×10^{15} molecules/cm²) are found in densely populated cities, such as Lahore, Delhi, Varanasi, and Dhaka in the IGP, as well as Guangzhou and Shenzhen, Chongqing in South Central China, Chengdu in Sichuan, Seoul in South Korea and Tokyo in Japan (Fig. 1c and Fig. S1 in Supplementary). Elevated NO_2 concentrations are also prominent in heavily industrialized regions, notably the North China Plain (NCP) and the industrial complexes and coalfields located in the eastern Indian states of Chhattisgarh, Jharkhand, and Odisha, part of the Indian coal belt. Despite these shared characteristics, East Asia exhibits a significantly larger extent of high NO_2 concentrations, explaining its higher average value compared to South Asia (4.4×10^{15} molecules/cm² vs. 1.9×10^{15} molecules/cm²). Similarly, SO_2 hotspots are also observed in these sub-regions, as they are associated with heavy industry and coal-fired power plants (Fig. 1e). In South Asia, these hotspots are prominently visible over the eastern Indian coal belt, whereas in East Asia, they are primarily located in the Sichuan Basin, the Ningxia province and the Beijing-Tianjin-Hebei region. While regional mean values for SO_2 remain relatively low due to the highly localized nature of its emissions (0.04 DU for South Asia and 0.06 DU for East Asia), concentrations within these specific hotspots can exceed 0.2 DU.

CO, NO_2 and SO_2 trends illustrated in Fig. 1b, 1d, 1f and summarized in Fig. 3, reveal a clear divergence between South Asia and East Asia: a steady increase is observed in South Asia for all three pollutants, while East Asia exhibits a significant and widespread decline. This contrast is first evident for CO, where South Asia exhibits a positive and significant trend of +3.9 ± 1.1 %/dec whereas East Asia shows a negative and significant trend of -9.4 ± 1.7 %/dec. The NCP and Sichuan Basin display the most pronounced declines (< -10 %/dec), while the increasing trend in South Asia appears more regionally homogeneous (Fig. 1b). We also observe a similar contrasting pattern in NO_2 trends between the two regions, though with greater magnitude than for CO (Fig. 1d). Specifically, South Asia exhibits a significant upward trend (+12.4 ± 2.1 %/dec) whereas East Asia is characterized by a significant downward trend (-22.5 ± 4 %/dec). Fig. 1f also shows divergent pattern in SO_2 trends between South Asia and East Asia. A significant negative trend of -84.6 ± 16.3 %/dec is found over East Asia, while South Asia shows a positive significant trend of 14.4 ± 3.5 %/dec. We also notice from Fig. 1f that trends are spatially less homogenous in comparison to CO, especially for South Asia. The significant and increasing trends are mainly located over the Eastern Indian coal belt, consistent with the intensified activity and expansion of coal-fired power plants found in the region (Fioletov et al., 2023).

These divergent satellite-observed trends align with the evolution of anthropogenic emissions of CO, NO_x, and SO_2, as given by the CAMS-GLOB-ANT inventory (Fig. S2 in Supplement). In contrast, no divergence between East Asia and South Asia is observed in biomass burning emissions of CO and NO_x, with decreases observed in both regions according to the GFAS inventory (Fig. S3 in Supplement). However, biomass burning represents a smaller contribution than anthropogenic emissions. For example, CO emissions from local anthropogenic sources are approximately 7 and 20 times larger than those from biomass burning over South and East Asia, respectively, suggesting a dominant role of anthropogenic sources in driving the observed

https://doi.org/10.5194/egusphere-2026-4393
Preprint. Discussion started: 17 August 2026

regional trends. The decline in local fire emissions may have contributed to the decreasing trends observed over East Asia but cannot explain the increasing trends observed over South Asia.

Both South Asia and East Asia generally present high values of AOD (0.42 and 0.47, respectively), implying a high aerosol loading in these regions, as shown in Fig. 1g. However, within each region, specific areas exhibit even higher values, such as the IGP in South Asia, and the NCP and Sichuan Basin in East Asia, where average AOD exceed 0.75. While AOD only provides an indication of the total aerosol loading and not its specific chemical composition, its spatial distribution coincides with those of CO, NO_2 and SO_2, suggesting a predominantly anthropogenic nature for the aerosols in the regions. However, mineral dust transport can also influence the observed AOD, particularly in South Asia through emissions from arid regions surrounding the Indian subcontinent and the Thar Desert (Jain et al., 2025; Prasad and Singh, 2007), and in East Asia through the Taklamakan and Gobi Deserts (Chen et al., 2025c), although this contribution is generally more episodic and strongly modulated by wind conditions compared with the more continuous contribution of anthropogenic emissions.

Same as CO, NO_2 and SO_2, a significant positive trend is found in South Asia (+9.2 ± 1.7 %/dec), while East Asia shows a significant negative trend (-32.2 ± 1.8 %/dec, Fig. 1h and 3). The consistency between AOD and gaseous pollutant trends suggests a substantial contribution from anthropogenic sources to aerosol changes, particularly in East Asia where the decline is most pronounced. This decrease is also consistent with the reduction in dust optical depth observed over Eastern China, especially during March–May (Liu et al., 2024). In South Asia, the AOD trend shows notable spatial heterogeneity (Fig. 1g) : while the majority of the Indian Peninsula exhibits a significant increasing trend, the Thar Desert shows a significant decline, previously reported by Pandey et al. (2017). This was attributed to a reduced dust loading associated with increased precipitation during the pre-monsoon season (March-May).

3.2. Surface temperature responses to air pollution changes and associated radiative processes

Aerosols have an influence on cloud formation and land surface temperature (T_{skin}) through both direct and indirect radiative effects, which alter the amount of incoming shortwave radiation reaching the surface ($SSW_{\downarrow}$). T_{skin} is also modulated by land surface properties such as vegetation changes, represented here by NDVI. Figure 2 illustrates the spatial distribution of cloud fraction, clear-sky $SSW_{\downarrow}$, T_{skin} and NDVI across Asia, averaged over the 2008-2025 period in panels a, c, e and g, respectively. Their corresponding annual trends, calculated at a 1×1° spatial resolution, are given in panels b, d, f and h. Note that we show here only T_{skin} average and trends over 2008-2025 from IASI daytime observations in Fig. 2e and 2f.

https://doi.org/10.5194/egusphere-2026-4393
Preprint. Discussion started: 17 August 2026

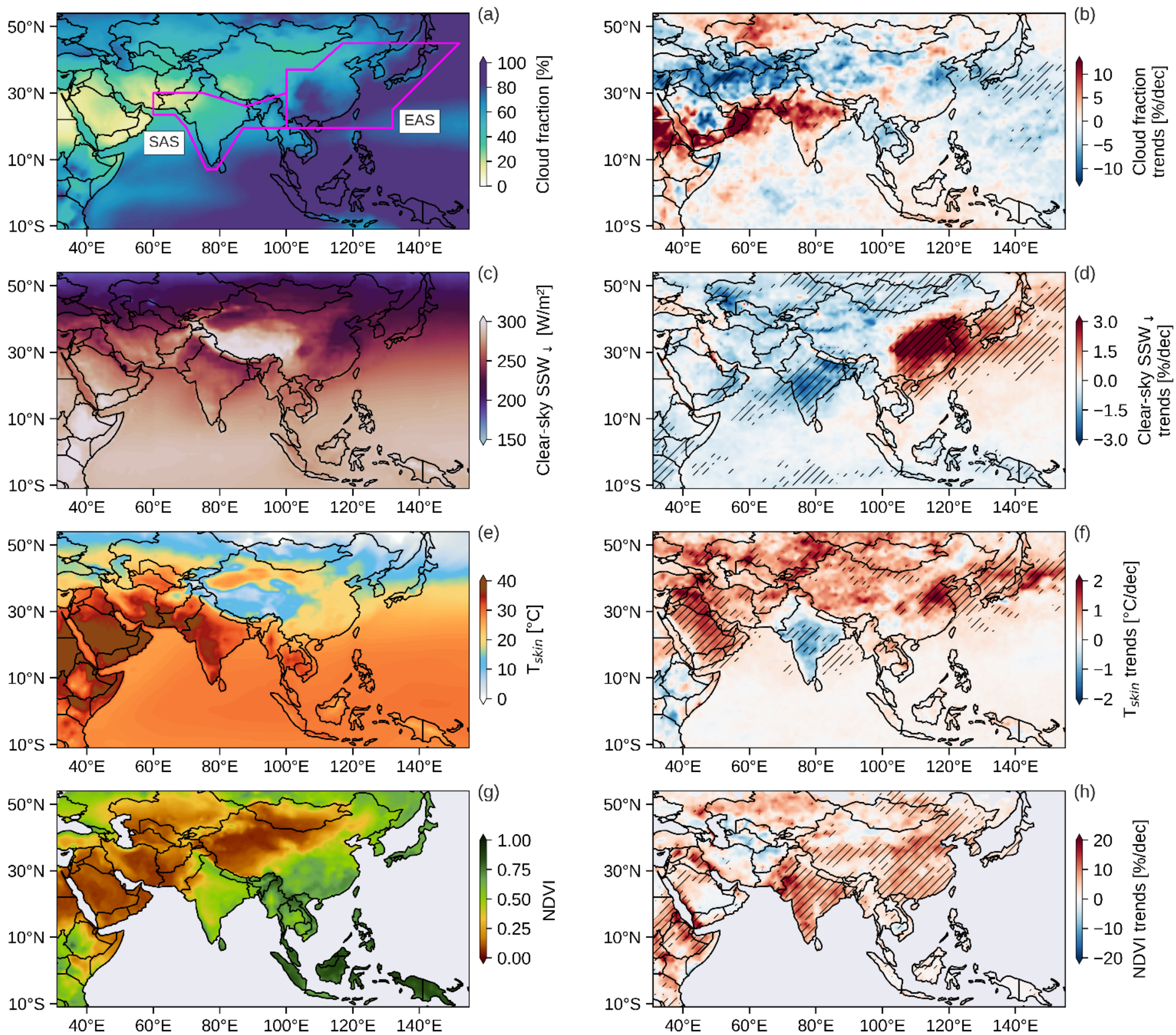

Figure 2. Left column (top to bottom): spatial distribution of cloud fraction (a), clear-sky $SSW_{\downarrow}$ (c), T_{skin} (e), and NDVI (g) averaged over 2008-2025. Right column (top to bottom): corresponding trends at a 1×1° spatial resolution for cloud fraction (b), clear-sky $SSW_{\downarrow}$ (d), T_{skin} (f) and NDVI (h) over 2008-2025. Hatched areas indicate statistically significant trends. East Asia (EAS) and South Asia (SAS) are delimited by the solid lines in magenta on panel (a).

From Fig. 2a, we observe an overall higher cloud fraction in East Asia than in South Asia (69% vs. 42%). South Asia includes areas with low cloud fraction, reaching down to 20% in the arid areas of Southern Pakistan. In contrast, East Asia contains areas with much higher cloud fraction exceeding 80%, such as South-Central China and the Sichuan Basin.

Figure 2c shows that East Asia presents a lower average clear-sky $SSW_{\downarrow}$ compared to South Asia (241 vs. 260 W/m²), which is partly due to the higher latitudes of the region. Beyond this latitudinal effect, significant spatial variations within each region

https://doi.org/10.5194/egusphere-2026-4393
Preprint. Discussion started: 17 August 2026

can be linked to high aerosol loading. This is particularly evident in the NCP and the IGP, both of which exhibit reduced radiation with clear-sky SSW↓ values dropping to approximately 220 W/m².

Same as clear-sky SSW↓, South Asia records a significantly higher average T_{skin} than East Asia (31°C vs. 18.2°C, Fig. 2e). T_{skin} is spatially more homogenous in East Asia than in South Asia, where a thermal gradient is observed from higher temperatures in Southern Pakistan toward lower temperatures in Central India.

These climatic features are also closely coupled with surface vegetation. South Asia presents a lower mean NDVI than East Asia (0.46 vs. 0.55, Fig. 2e), reflecting the larger extent of semi-arid and arid regions (Southern Pakistan, Thar desert). The remaining vegetated areas are largely dominated by croplands, while forests are mainly located in Central and Eastern India and Myanmar (Reddy et al., 2020). East Asia is characterized by a mosaic of intensive agricultural areas, such as the NCP, and dense forests regions mainly located in Central and Southern China (Yang and Huang, 2021).

Similarly to the diverging trends in gaseous pollutants and aerosols, we observe a marked contrasting pattern of cloud fraction, SSW↓ and T_{skin} trends across Asia (Fig. 2b, 2d and 2f). Over the 2008-2025 period, South Asia exhibits a widespread positive trend in cloud fraction, at a rate of +4.3 ± 2.3 %/dec, where East Asia shows a moderate decline of -1.5 ± 1.1 %/dec (Fig. 3). Although not statistically significant, trends in cloud fraction are consistent with the observed trends in AOD, supporting the relationship between aerosols and cloud formation.

Regarding clear-sky SSW↓, a significant negative trend is found over South Asia, whereas a significant positive trend is observed over East Asia (-1.1 ± 0.1 vs. +1.2 ± 0.4 %/dec, Fig. 3). Similar trend directions but of greater magnitude are observed for all-sky SSW↓ (Fig. S4 in Supplement). Because of the difference in overpass times between CERES and IASI, and to ensure better temporal consistency for T_{skin} trends which are dependent on the hour of day (Safieddine et al., 2025), we conducted a supplementary analysis using clear-sky SSW↓ from the MERRA-2 reanalysis. The spatial distribution and the associated trends of MERRA-2 clear-sky SSW↓ spatially and temporally matched to IASI daytime overpass at clear-sky conditions are shown in Fig. S5 (Supplement). We find the same regional trend directions as in Fig. 3d, though with different magnitude. Overall, across all SSW↓ datasets, the same regional trend pattern is found, regardless of whether clear-sky or all-sky conditions are considered, or the time of the day.

The same regional trend pattern is observed for daytime IASI T_{skin} (Fig. 2f). South Asia shows a non-significant negative trend of -0.2 ± 0.2 °C/dec (Fig. 3), although most of the Indian Peninsula shows strong and significant negative trend while the IGP (except Bangladesh) exhibits a non-significant and very weak negative trend. East Asia shows a positive significant trend of +0.6 ± 0.1 °C/dec (Fig. 3) with trends being the strongest over the NCP, where they are also significant (Fig. 2f). In contrast to the daytime trends, no diverging pattern is found across Asia during the night and both South and East Asia exhibit positive trends (+0.4 ± 0.1 °C/dec and +0.8 ± 0.1 °C/dec, respectively, Fig. 3). When considering the combined daytime and nighttime T_{skin}, the regional contrast persists, with a significant warming in East Asia (+0.7 ± 0.1 °C/dec) and near-zero non-significant trend in South Asia (0.0 ± 0.1 °C/dec, Fig. 3). The spatial distribution of the nighttime and combined daytime and nighttime T_{skin} trends are shown in Fig. S6 (Supplement). The combined daytime and nighttime trends still reveal a clear coverage of negative values over the Indian Peninsula, same as the trends observed in the daytime-only observations (Fig. 2f). A similar

https://doi.org/10.5194/egusphere-2026-4393
Preprint. Discussion started: 17 August 2026

but weaker pattern is observed for MERRA-2 T_{2m} sampled at IASI overpass times (Fig. S7, Supplement), indicating that these temperature changes extend beyond the surface into the lower atmosphere.

In contrast to the other studied variables, NDVI exhibits a positive trend across both South and East Asia (Figs. 2h and 3), consistent with the widespread greening reported over recent decades (Chen et al., 2019). This greening is mainly attributable to human-induced land management, including forest expansion in East Asia (China) and cropland expansion in both South and East Asia (India and China, Kuttippurath and Kashyap, 2023; Wang et al., 2025).

Vegetation greening generally exerts a cooling effect on surface temperature during the day through changes in surface energy balance, mainly via evapotranspiration and albedo. Over the Indian Peninsula, vegetation greening is associated with decreasing T_{skin} (Fig. 2f and 2h), which could be linked to enhanced evapotranspiration driven by increased soil moisture from irrigated croplands (Ambika and Mishra, 2019). In contrast, East Asia shows a positive T_{skin} trend despite a widespread greening, indicating that the biophysical effects of vegetation alone are not sufficient to explain regional T_{skin} trends. This suggests a potential contribution from atmospheric factors: in South Asia, the cooling effect of greening acts in synergy with increasing AOD and cloud fraction (reducing $SSW_{\downarrow}$), whereas in East Asia, declining AOD and cloud fraction (increasing $SSW_{\downarrow}$) reinforce regional warming despite widespread greening.

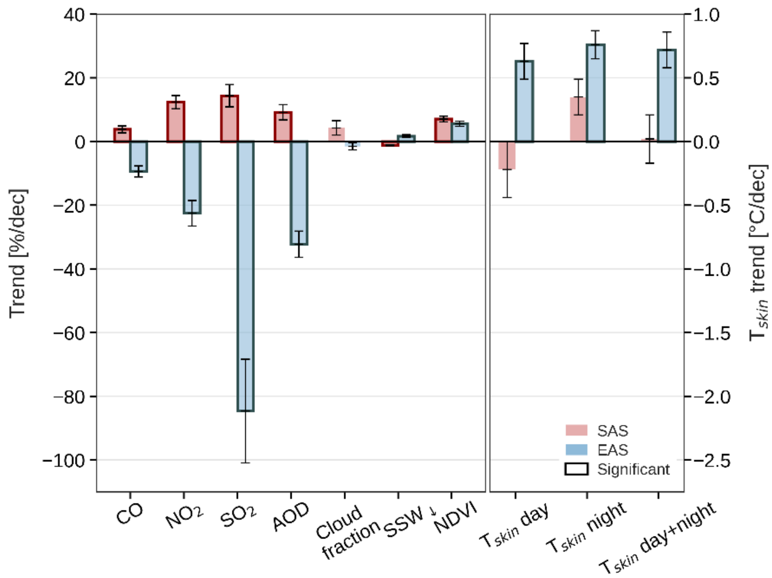

Figure 3. Regional trend values of CO, NO_2, SO_2, AOD, cloud fraction, clear-sky $SSW_{\downarrow}$, NDVI (in %/dec, left axis) and day-only, night-only, day and night combined T_{skin} (in °C/dec, right axis), for South Asia (SAS, in pink) and East Asia (EAS, in blue). Trend standard errors are shown as error bars. Significant trends are indicated by thicker contours.

https://doi.org/10.5194/egusphere-2026-4393
Preprint. Discussion started: 17 August 2026

4. Evaluation of CMIP6 simulations: which scenario captures the observed present-day trend pattern between South Asia and East Asia?

We first evaluate which SSP best reflects the divergent observational patterns between South and East Asia discussed above, in order to examine how selected CMIP6 models simulate air pollution and surface temperature changes for the present-day (2008-2025). Since the historical simulations end in 2014, we show in Fig. 4 the relative changes between 2015-2025 and 2008-2014 for CO, NO_2 and SO_2 concentrations, AOD and surface temperature (from top to bottom) over Asia, as depicted by satellite observations (first column) and the CMIP6 multi-model mean under SSP1-2.6 (second column), SSP2-4.5 (third column), and SSP3-7.0 (fourth column). As mentioned previously, these SSPs were selected to cover a range of different future trajectories, spanning from a strong pollution control scenario (SSP1-2.6) to a weak one (SSP3-7.0). Changes between the present-day and the historical period are expressed in %, except for surface temperature, which are given in °C. Same as in Fig. 1d and 1f, the relative changes in NO_2 and SO_2 (Fig. 4e and 4i) are only displayed for grid cells where the average concentration over 2008-2014 exceeds 0.5×10^{15} molecules/cm^2 and 0.01 DU, respectively. The relative changes in IASI surface temperature (T_{skin}) presented in panel (q) are derived from combined daytime and nighttime observations to ensure a consistent comparison with the monthly mean outputs provided by the CMIP6 models. The relative changes values for each variable, region and dataset (satellite observations and simulations) are summarized in Table 2.

https://doi.org/10.5194/egusphere-2026-4393
Preprint. Discussion started: 17 August 2026

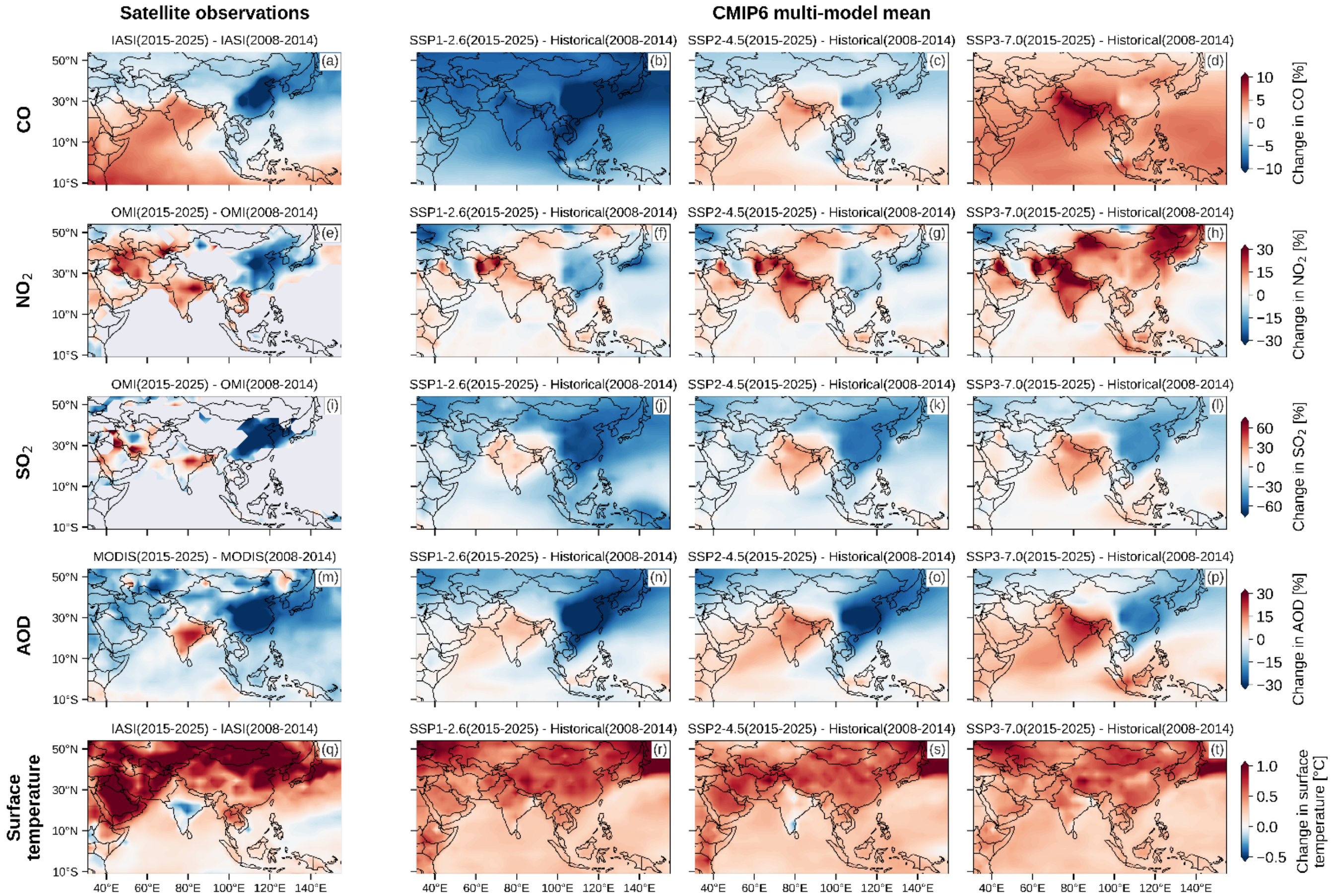

Figure 4: Observed and simulated relative changes (2015-2025 vs. 2008-2014) in CO, NO_2 and SO_2 concentrations, AOD and surface temperature (top to bottom) at a 3×3° spatial resolution. The first column shows changes from satellite observations (IASI, OMI, MODIS), while the subsequent columns show changes from the CMIP6 multi-model mean under SSP1-2.6 (second column), SSP2-4.5 (third column), and SSP3-7.0 (fourth column). Note that the changes in IASI surface (skin) temperature presented in panel (q) are derived from combined daytime and nighttime observations.

For CO, the observed divergent pattern between South and East Asia is only reproduced under SSP2-4.5, whereas SSP1-2.6 and SSP3-7.0 show an across overall decrease and increase across Asia, respectively (Fig. 4a-d). However, the simulated changes in CO concentrations under SSP2-4.5 is less pronounced than that observed with IASI. The observed decline in East Asia is closer to the SSP1-2.6 projection than to SSP2-4.5, while the observed increase in South Asia is more aligned with the moderate growth of SSP2-4.5 (Table 2). Simulated changes are consistent with the annual relative emission trajectories shown in Fig. S8a and S8b (Supplement). Over the 2015-2025 period, CO emissions in East Asia decrease in both SSP1-2.6 and SSP2-4.5 but at different rates (more pronounced in SSP1-2.6), while they show a slight increase in SSP3-7.0. For South Asia, we note an increase in CO emissions both in SSP2-4.5 and SSP3-7.0, while a decline is observed only for the SSP1-2.6 scenario.

https://doi.org/10.5194/egusphere-2026-4393
Preprint. Discussion started: 17 August 2026

Contrasting changes in NO_2 concentrations as observed by OMI are reproduced under SSP1-2.6 and SSP2-4.5, while an increase of NO_2 is simulated over all Asia in SSP3-7.0 (Fig. 4e-h). South Asia experiences an increase of NO_2 in all SSPs, with SSP3-7.0 presenting the largest increase (Table 2). The observed relative change in South Asia falls between SSP1-2.6 and SSP2-4.5, while in East Asia, it aligns most with SSP1-2.6, although the multi-model mean still underestimates the magnitude of this decline (Table 2). The regional differences in the scenarios are explained by the NO_x emission trajectories (Fig. S8c and S8d, Supplement). In South Asia, NO_x emissions increase under all SSPs over 2015–2025. In East Asia, NO_x emissions strongly decrease under SSP1-2.6 and SSP2-4.5, which is consistent with the simulated NO_2 concentration changes shown in Fig. 4.

For SO_2, a contrasting pattern between East and South Asia is evident in all SSPs, although the magnitudes differ significantly (Fig. 4i-l and Table 2). The changes in SO_2 concentration in both regions as observed by OMI are the closest to the SSP1-2.6 projection. However, the observed changes exhibit stronger spatial heterogeneity than the model simulations, particularly in South Asia, where the increase is mainly driven by the eastern Indian coal belt (Fig. 4i). Overall, the simulated concentration changes are consistent with the SO_2 emissions trajectories: all SSPs show a continued increase in SO_2 emissions for South Asia, whereas a consistent decline is noted for East Asia (Fig. S8e and S8f).

A characteristic diverging pattern in AOD is found in all studied SSP, but with varying magnitudes (Fig. 4m-p). AOD increases in South Asia following the severity of the SSP, while in East Asia, the magnitude of the decrease weakens from SSP1-2.6 to SSP3-7.0 (Table 2). Over South Asia, the observed increase in AOD by MODIS falls between SSP1-2.6 and SSP2-4.5. However, this regional mean hides spatial heterogeneity: the northern part of South Asia exhibits an observed negative change, while most of the Indian Peninsula shows an increase (~30%) closer to SSP3-7.0 (Fig. 4m). In contrast, MODIS shows a more homogeneous decline in East Asia, with a magnitude lying between SSP1-2.6 and SSP2-4.5 (Table 2).

Unlike gaseous pollutants and AOD, no diverging pattern in surface temperature changes between South and East Asia is found for any of the studied SSPs (Fig. 4q-t). While CMIP6 simulations do not reproduce the sharp regional divergence seen in IASI observations, they consistently simulate stronger warming in East Asia than in South Asia across all SSPs (Table 2). The lowest average surface temperature change over South Asia is simulated under SSP2-4.5, while the highest warming over East Asia occurs under SSP1-2.6.

To better understand the regional differences in simulated temperature changes, we further examine clear-sky $SSW_{\downarrow}$ changes across the different SSPs given in Fig. S9 (Supplement). Changes in clear-sky $SSW_{\downarrow}$ are consistent with the simulated AOD across all SSPs, with an increasing (decreasing) clear-sky $SSW_{\downarrow}$ in East Asia (South Asia). While surface temperature changes in East Asia are consistent with the magnitude of the simulated AOD and clear-sky $SSW_{\downarrow}$ changes in all SSPs (i.e. decreasing warming with increasing AOD), this relationship is less straightforward over South Asia. Despite a continuous increase in AOD across the SSPs and a corresponding and intensifying reduction in clear-sky $SSW_{\downarrow}$, South Asia does not exhibit a proportional attenuation of surface temperature. Localized areas of weak negative changes or near-zero changes are nevertheless observed over parts of South India in SSP2-4.5 and the eastern part of the IGP under SSP3-7.0 (Figures 4s and 4t). We investigated the origin of this spatial heterogeneity by examining the changes in surface temperature as simulated by each individual model (Figure S10, Supplement). We observe that an overall negative change of surface temperature is only visible for the GFDL-ESM4 simulation and a weak (near-zero) change in surface temperature for MRI-ESM-2-0 and UKESM1-0-LL, explaining the average limited warming over South Asia under SSP2-4.5.

Relative changes	Region	Satellite observations	SSP1-2.6	SSP2-4.5	SSP3-7.0
CO (%)	SAS	+3.7	-7.9	+2.7	+7.2
	EAS	-8.2	-11.2	-3.5	+3.5
NO_2 (%)	SAS	+10.7	+5.5	+14.1	+19.2
	EAS	-17.9	-11.7	-8.4	+12.5
SO_2 (%)	SAS	+10.2	+7.0	+17.6	+22.4
	EAS	-63.5	-56.8	-45.9	-36.4
AOD (%)	SAS	+7.1	+5.5	+11.2	+16.1
	EAS	-27.1	-30.3	-25.5	-16.2
Surface temperature (°C)	SAS	+0.14	+0.41	+0.25	+0.37
	EAS	+0.74	+0.62	+0.59	+0.55

Table 2. Regional mean changes in CO, NO_2 and SO_2 concentrations, AOD and surface temperature between 2015-2025 and 2008-2014 over South Asia (SAS) and East Asia (EAS), from satellite observations (IASI, OMI and MODIS) and the CMIP6 multi-model mean under the SSP1-2.6, SSP2-4.5 and SSP3-7.0 scenarios.

5. Future changes in air pollution and surface temperature in South Asia and East Asia under different scenarios

We now examine the long-term trajectories of air pollutants and surface temperature to see how the regional disparities discussed above evolve throughout the 21st century, under the different scenarios. Figure 5 presents the regional time series of CO, NO_2 and SO_2 concentrations, AOD and surface temperature changes relative to the 2008-2014 period up to 2100, from top to bottom. Results are shown for South and East Asia in the left and right columns, respectively. Observed changes from satellite instruments are represented by the black curves, while simulated changes from the CMIP6 multi-model mean are shown for in blue for the historical simulation, in green for SSP1-2.6, in yellow for SSP2-4.5, and in red for SSP3-7.0. Shaded areas around each curve corresponds to the inter-model variability. Same as Fig. 4, yearly changes are expressed in % except for surface temperature which is given in °C. Changes in IASI surface temperature (T_{skin}, Fig. 5i and 5j) are derived from combined daytime and nighttime observations to ensure a consistent comparison with the monthly mean outputs of the CMIP6 models.

https://doi.org/10.5194/egusphere-2026-4393
Preprint. Discussion started: 17 August 2026

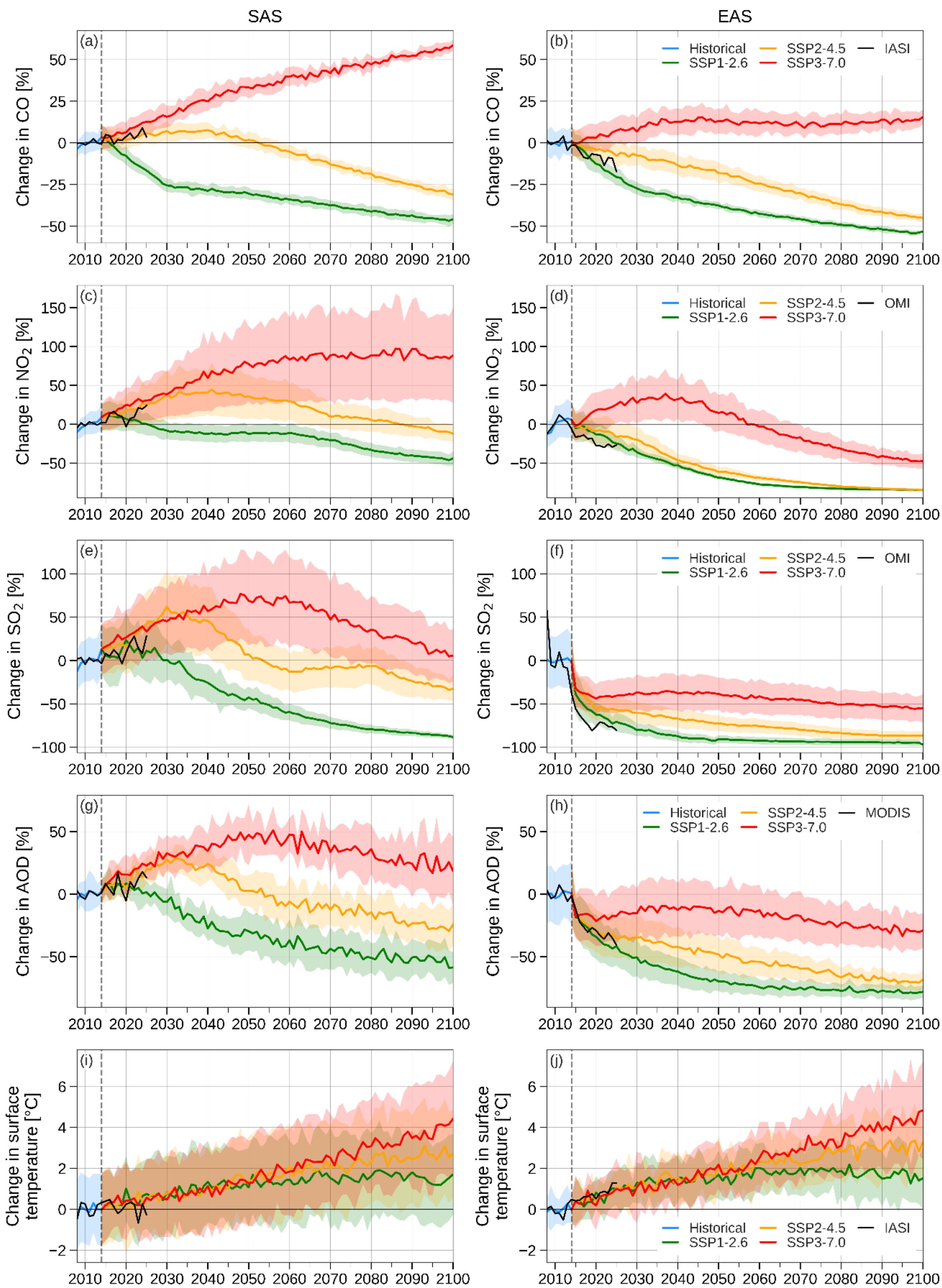

https://doi.org/10.5194/egusphere-2026-4393
Preprint. Discussion started: 17 August 2026

Figure 5: Regional changes predicted up to 2100 in CO, NO_2, and SO_2 concentrations, AOD and surface temperature relative to 2008-2014 (top to bottom) for South Asia (SAS, left column) and East Asia (EAS, right column). Observed changes from satellite instruments are represented by the black curves. Simulated changes from the CMIP6 multi-model mean are shown for the historical simulation in blue, SSP1-2.6, in green, SSP2-4.5, in yellow and SSP3-7.0, in red. Shaded areas around each curve correspond to the inter-model variability. The vertical dotted line at 2014 in each subplot marks the transition from the historical simulation to the SSPs.

Future regional changes of CO, NO_2 and SO_2 concentrations from the CMIP6 multi-model average generally follow the emissions trajectories as defined in each SSP (Fig. 5a-f and S8). Our analysis over 2015-2025 in Sect. 4 showed that CO concentration changes in South Asia closely align with the moderate increase projected by SSP2-4.5. The observed changes from IASI in Fig. 5a further support this consistency, showing a similar evolution to SSP2-4.5 until 2025. Under this scenario, CO concentrations are projected to increase until 2040 before declining toward 2100, reaching a reduction of -31% (Fig. 5a). SSP1-2.6 shows a similar long-term decline, but with an earlier decrease starting in 2015 and reaching -46% by 2100. A similar evolution is observed in East Asia, where satellite observed changes over 2015-2025 are consistent with the SSP1-2.6 trajectory characterized by a continuous decrease in CO concentrations throughout the century and reaching a reduction of -53% by 2100 (Fig. 5b). Under SSP2-4.5, East Asia exhibits a continuous decline in CO starting in 2015, in contrast to South Asia. However, under SSP3-7.0, the regions show contrasting evolutions: CO concentrations in South Asia are projected to rise drastically and continuously until 2100 (+59%), whereas in East Asia, they remain stagnant after 2040, reaching +16% by 2100, despite a decline in CO emissions (Fig S8b).

For NO_2, our analysis of the 2015-2025 period suggested South Asia was positioned between SSP1-2.6 and SSP2-4.5. Figure 5c indicates the satellite-observed evolution is more closely aligned with SSP2-4.5 than SSP1-2.6. Despite contrasting near- and mid-term trajectories, with NO_2 concentrations decreasing from 2025 onwards under SSP1-2.6 and peaking around 2040 under SSP2-4.5, both scenarios project a long-term decline by 2100 (-44% and -12%, respectively). In contrast, the SSP3-7.0 scenario for South Asia leads to a continuous increase by 2100 (+88%). Regarding East Asia, NO_2 is projected to decline by 2100 under all scenarios. While this reduction begins immediately in 2015 under SSP1-2.6 and SSP2-4.5, it is delayed until 2040 under SSP3-7.0, following the emission trajectory depicted in Fig. S8d. By the end of the century, NO_2 concentrations decrease by approximately -85% under SSP1-2.6 and SSP2-4.5, and -47% under SSP3-7.0.

SO_2 concentration changes in Fig. 5e and 5f reveal distinct regional evolutions throughout the 21st century. Satellite-observed changes in South Asia seem to be the closest to the SSP1-2.6 trajectory over 2015-2025 (Fig. 5e), although all SSPs project an increase in SO_2 concentrations until 2030 but at varying magnitude (+1% under SSP1-2.6, +62% under SSP2-4.5 and +45% under SSP3-7.0). After 2030, a clear divergence emerges between the SSPs. While SSP1-2.6 leads to a continuous decline through 2100 (-88%), SSP2-4.5 exhibits a more complex pattern, where SO_2 concentrations decrease between 2030 and 2050 but subsequently stagnate from 2060 to 2080. This is explained by the temporary rebound in emissions (Fig. S8e) before the downward trend resumes after 2080, reaching a change of -32% in 2100. Under SSP3-7.0, SO_2 changes peak around 2050, followed by a gradual decrease toward the end of the century (+5% in 2100). In contrast, East Asia region shows a consistent decline in SO_2 concentrations across all three SSPs, with the most pronounced reduction occurring under SSP1-2.6 (-97% in 2100), whose early trajectory is most consistent with the satellite-observed changes over 2015-2025, as discussed above.

https://doi.org/10.5194/egusphere-2026-4393
Preprint. Discussion started: 17 August 2026

Future AOD changes generally follow the trajectories to those of gaseous pollutants discussed above within each region (Fig. 5g and 5h). As discussed in the previous section, MODIS data revealed that average AOD changes over 2015-2025 in both South and East Asia fall between the SSP1-2.6 and SSP2-4.5. However, for South Asia, these two scenarios follow different trajectories during the first half of the century. While SSP1-2.6 shows a consistent decline starting from 2015 and reaching -58% by 2100, SSP2-4.5 exhibits an AOD increase until 2030 (+34%), followed by a decrease through 2100 (-59%). This mirrors the SO_2 trajectories under SSP2-4.5 and, to a lesser extent, NO_2 and CO (both of which peak around 2040). In contrast, under SSP3-7.0, AOD increases until 2050 before declining very gradually, although the AOD change remains positive in 2100 (+19%). In East Asia, AOD declines across all SSPs starting from 2015, though the magnitude of these reductions varies significantly by the end of the century (-78% for SSP1-2.6, -68% for SSP2-4.5, -29% for SSP3-7.0). The AOD trajectories closely mirror those of SO_2 in all three scenarios. The similarity is less evident for NO_2, particularly in SSP3-7.0, where NO_2 levels increase during the first half of the century. This suggests that sulfate aerosols represent a dominant component of aerosol composition in East Asia.

For surface temperature, the multi-model mean projects a continuous increase throughout the century in both regions (Fig. 5i and 5j), in contrast to the observational analysis presented in Sect. 3 and 4. Warming values remain relatively consistent across all scenarios until mid-century, after which the trajectories diverges after 2050, reaching in South Asia +1.7°C under SSP1-2.6, +2.7°C under SSP2-4.5, and +4.4°C under SSP3-7.0 by 2100. This divergence after 2050 coincides with the moderate and high decrease in AOD under SSP2-4.5 and SSP3-7.0, respectively. However, this trend is also explained by the CMIP6 scenario design, as greenhouse gas emissions (CO_2 and CH_4) diverge more sharply across the SSPs after the middle of century (Gidden et al., 2019). This explains also why the same observation can be made for EAS, where surface temperature changes also seem to diverge after 2050, with end-of-century warming levels ranging from +1.5°C to +4.8°C (Fig. 5j).

Interestingly, we find a larger inter-model spread in surface temperature changes over South Asia starting as early as 2015, whereas East Asia exhibits a spread that increases more gradually throughout the century in all SSPs. In South Asia, the highest warming is simulated by UKESM1-0-LL, with values ranging from +4.3°C (SSP1-2.6) to +8.3°C (SSP3-7.0) by 2100. The lowest warming is projected by GFDL-ESM4, with values reaching only +0.3°C to +2°C. This difference in model is also observed in EAS (+3.5-8°C for UKESM1-0-LL and +0.02-2.5°C for GFDL-ESM4). These discrepancies are consistent with the known characteristics of these models: UKESM1-0-LL features a high effective climate sensitivity, whereas GFDL-ESM4 and MRI-ESM2-0 are characterized by lower sensitivities (Wang et al., 2021a).

6. Conclusion and discussion

This study documents and analyzes present-day and future air pollution and surface temperature trends in South Asia and East Asia relying on satellite observations and climate simulations. By examining the full chain of processes considered in this study, from gaseous pollutants and aerosols to cloud cover and surface shortwave radiation, we provide an integrated view of how air quality changes are associated with regional surface temperature trends. To do so, we used long-term, high-quality

https://doi.org/10.5194/egusphere-2026-4393
Preprint. Discussion started: 17 August 2026

and continuous satellite measurements of atmospheric composition and surface temperature, which provide a robust observational baseline for evaluating climate model simulations through direct comparison with both recent historical simulations and future projections. Since CMIP6 historical experiment ends in 2014, the subsequent decade (2015-2025) provides a unique opportunity to assess which trajectories are most consistent with recent observations over South and East Asia. Comparing current satellite observations trends with SSP projections (SSP1-2.6, SSP2-4.5 and SSP3-7.0) allows for a more nuanced discussion of the regional air pollution-temperature relationship, which often diverges from the global averages typically reported in the literature (Forster et al., 2026).

Satellite observations show that South and East Asia have undergone contrasting changes in air quality over 2008-2025, with a significant decline in CO, NO_2, SO_2 and AOD in East Asia, as opposed to an increase in South Asia. The observed air pollution trends are consistent with previous studies reporting contrasting changes in atmospheric composition across South and East Asia over recent decades (Rahman et al., 2023). However, for CO, while Buchholz et al. (2021) reported decreasing trends from MOPITT over 2002-2018 for South Asia, we find a significant increase over 2008-2025. This difference highlights the importance of considering recent changes in atmospheric composition when evaluating regional pollution trends. These air pollution trends, particularly aerosol trends, affect regional cloud fraction and incoming surface shortwave radiation, subsequently affecting surface temperature. We find a daytime cooling and a nighttime attenuated warming over South Asia and a strong significant warming in East Asia, both consistent with observed cloud fraction and surface shortwave radiation trends. However, cloud fraction and skin temperature trends over South Asia are not statistically significant, suggesting that high interannual variability of clouds and temperature, potentially associated with large-scale phenomena like ENSO or the Asian monsoon (not discussed here), can mask the long-term signal over the 18-year time study period (Santer et al., 2011). Nevertheless, significant daytime cooling is observed over large parts of India, indicating that robust regional signals can still emerge despite the lack of significance in the regional mean. Vegetation changes further modulate these trends, but the observed temperature divergence suggests that biophysical cooling from greening is either synergistic with aerosol-induced cooling in South Asia or outweighed by increased surface solar radiation in East Asia.

Beyond characterizing recent changes, comparing observations with CMIP6 simulations provides insight into whether present-day air quality changes and their associated climate responses are consistent with the trajectories represented in current scenarios. The observed regional differences between South and East Asia are reproduced under specific SSPs for CO and NO_2, while for SO_2 and AOD, contrasting regional changes are found in all scenarios. AOD trends in South and East Asia have also been examined in CMIP6 simulations against MODIS observations by Ramachandran et al. (2022). They showed that, although the multi-model mean under SSP2-4.5 did not reproduce the observed contrasting pattern, some individual models, including those selected in our study, captured a weak negative AOD trend over parts of East Asia during 2002-2018. Our analysis extends these previous assessments by evaluating which SSP trajectories are most consistent with recent satellite-observed changes, including gaseous pollutants. We find that the rapid decline of gaseous pollutants in East Asia aligns most closely with the SSP1-2.6 trajectory, whereas South Asia lies between SSP1-2.6 (for SO_2) and SSP2-4.5 (for CO and NO_2). For AOD, both regions show changes positioned between SSP1-2.6 and SSP2-4.5 in terms of magnitude and the sign of the

https://doi.org/10.5194/egusphere-2026-4393
Preprint. Discussion started: 17 August 2026

changes remain consistent with those of their gaseous precursors. For example, in East Asia, the similarity between AOD and SO_2 patterns suggests a strong sulfate contribution. This is consistent with Ren et al. (2024), who showed that sulfate represents a large fraction of simulated $PM_{2.5}$ over East Asia, particularly in the GFDL-ESM4 and MRI-ESM2-0 models.

However, the observed surface temperature pattern is not fully replicated in terms of magnitude and direction in the CMIP6 simulations, which can be partly explained by the design of the SSPs. While these pathways diverge significantly after 2050, surface temperature evolution over 2015-2025 mainly depends on the competition between regional aerosol cooling and warming from rising greenhouse gases concentrations (Gidden et al., 2019). The overall warming simulated in both regions suggests that greenhouse gas forcing dominates over aerosol effects during this period, partly explaining the weaker spatial contrast compared with observations.

Moreover, interpreting surface temperature as provided by Earth system models is challenging since it is a prognostic variable resulting from a multitude of interacting processes. Discrepancies between observed and simulated changes can thus arise from how these processes are represented across models, through parameterization, which introduce uncertainties in simulated surface temperature. This includes uncertainties stemming from aerosol representation, which depends on the aerosol cycle schemes implemented in each model as well as the underlying emission inventories. For instance, some studies have reported an overestimation of aerosol concentrations in East Asia, particularly for black carbon, due to overestimated emissions (Ikeda et al., 2023) whereas others have shown an underestimation of fine particulate matter ($PM_{2.5}$) concentrations partly attributed to an inadequate representation of nitrate and ammonium aerosols (Ren et al., 2024). This is particularly important as parts of Asia experience an increase in ammonia concentrations (Ismaeel et al., 2024; Van Damme et al., 2021). Accurate representation of aerosol composition is critical as different species have distinct effects on the radiation budget and surface temperature (Luo et al., 2025; Wang et al., 2021b). Furthermore, uncertainties in aerosol representation also propagate into aerosol-cloud interaction (ACI) schemes, which remain a major source of uncertainty in climate modelling due to limitations in observations and process understanding (Intergovernmental Panel On Climate Change, 2014). While ACI radiative forcing can exceed aerosol direct effects (Kalisoras et al., 2024; Smith et al., 2020), differences in how models simulate these interactions regionally can lead to substantial variability in regional cloud responses (Fig. S11, Supplement), despite relatively consistent spatial distribution of aerosols across models and scenarios (Fig. S12). Cloud properties are also influenced by a wide range of processes beyond aerosols (atmospheric dynamics, cloud microphysics, thermodynamics), further contributing to uncertainties in simulated radiation budgets.

Surface temperature depends not only on atmospheric processes but also on land-atmosphere exchanges, which are strongly influenced by energy and water cycles. Differences among models arise from the representation of both physical and biophysical land surface properties, including albedo, surface roughness, soil moisture, irrigation and vegetation structure associated with land cover definitions. These land properties can thereby modify the radiation budget and the partitioning of surface energy into sensible and latent heat fluxes, through evapotranspiration and hydrological processes (Li et al., 2021; Luo et al., 2024; Niu et al., 2019). Surface temperature is also modulated by exchanges with the lower atmosphere, especially through planetary boundary layer dynamics and turbulent mixing, which regulate sensible and latent heat fluxes and are thus themselves represented differently across models (Meng et al., 2023; Shin et al., 2018). It is also important to note that our analysis is based on three Earth system models and may not fully represent the entire CMIP6 ensemble.

While this study focuses on the impact of air pollution on surface temperature, changes in surface temperature also influences air pollution trends, whose future evolution remains uncertain due to a multitude of sources (Doherty et al., 2022). This includes future emissions, such as those from biomass burning, which are not interactive and are defined based on land management assumptions (Popp et al., 2017). Rising temperatures increase fire risks, leading to higher emissions of carbonaceous aerosols and other trace gases (Tian et al., 2023, 2025). Natural aerosol emissions, such as dust, are also expected to rise with increasing temperatures, alongside emissions of temperature-sensitive precursors like ammonia or biogenic volatile organic compounds, further contributing to the formation of secondary organic aerosols (Abeed et al., 2023; Gomez et al., 2023; Thornhill et al., 2021). Global and regional atmospheric dynamics (i.e. the Asian monsoon) and meteorological patterns are also reshaped under climate change, by increasing or decreasing atmospheric stability and thus directly impacting pollutants transport (Banks et al., 2022; Katzenberger et al., 2021; Paulot et al., 2022; Zhou et al., 2024).

Finally, this work highlights the importance of continuous air pollution monitoring in regions facing evolving and uncertain air quality challenges, with important implication for regional climate. This study is relevant in the context of the upcoming CMIP7 simulations, which will benefit from an extended historical period running through 2021 (Dunne et al., 2025). This extension will provide an opportunity to better evaluate model responses to recent observed changes (2015-2021), such as quantifying the radiative impact of aerosols over this period with a clearer separation between aerosol-driven changes and concurrent climate change. In CMIP6, such attribution is limited to the SSP3-7.0 scenario within AerChemMIP experiments (Collins et al., 2017), which may not fully represent present-day observed emission trajectories. More generally, current scenario frameworks remain constrained by their design, as they are not intended to capture abrupt changes associated with unforeseen events, such as the COVID-19 pandemic, and should be viewed as physically consistent storylines of possible evolution rather than deterministic representations of future atmospheric composition and climate. This highlights the inherent uncertainty in scenario-based projections and the need for continuous satellite monitoring to better evaluate and refine not only emission trajectories but also the interactions between climate and chemistry.

Data availability

- The IASI L2 Carbon Monoxide (CO) Climate Data Record (CDR) product is available on the EUMETSAT Data Store (https://user.eumetsat.int/catalogue/EO:EUM:DAT:0959) (AC SAF, 2024). Daily files generated from the CO CDR orbit files can be downloaded from the Aeris portal (http://iasi.aeris-data.fr/CO/), as well as the IASI L2 Carbon Monoxide NRT from Metop-B (https://doi.org/10.25326/64) and Metop-C (https://doi.org/10.25326/65). Last accessed on 2 February 2026.
- The IASI skin temperature and cloud detection products from Metop-A, -B and -C are available on https://iasi-ft.eu/ (Safieddine et al., 2020, 2026; Whitburn et al., 2022).

https://doi.org/10.5194/egusphere-2026-4393
Preprint. Discussion started: 17 August 2026

- OMI/Aura L2 Tropospheric NO_2 is derived from https://doi.org/10.5067/Aura/OMI/DATA2417 (Krotkov et al., 2024a) and SO_2 from https://doi.org/10.5067/Aura/OMI/DATA2422 (Krotkov and Li, 2025). Last accessed on 15 March 2026.
- Daily L3 AOD data from MODIS/Terra are available in http://dx.doi.org/10.5067/MODIS/MOD08_D3.061 (MODIS Atmosphere Science Team, 2015). Last accessed on 10 February 2026.
- Monthly NDVI data (MOD13A3) from MODIS/Terra can be downloaded from https://doi.org/10.5067/MODIS/MOD13A3.061 (Didan, 2021). Last accessed on 24 February 2026.
- The CERES EBAF dataset is obtained from the NASA Langley Research Center Atmospheric Science Data Center (https://doi.org/10.1175/JCLI-D-17-0523.1, Kato et al., 2018). Last accessed on 15 April 2026.
- Anthropogenic emissions from CAMS-GLOB-ANT are provided by https://permalink.aeris-data.fr/CAMS-GLOB-ANT (Soulie et al., 2024). Last accessed on 5 April 2026.
- Fire emissions from GFAS can be downloaded from the Copernicus Atmosphere Monitoring Service Atmosphere Data Store catalogue (https://doi.org/10.24381/a05253c7, Kaiser et al., 2012). Last accessed on 5 April 2026.
- MERRA-2 T_{2m} and clear-sky $SSW_{\downarrow}$ can be derived from https://doi.org/10.5067/VJAFPLI1CSIV and https://doi.org/10.5067/Q9QMY5PBNV1T respectively (Global Modeling And Assimilation Office, 2015b, a). Last accessed on 20 April 2026.
- CMIP6 model outputs from the historical experiment and SSP1-2.6, SSP2-4.5 and SSP3-7.0 were downloaded from https://metagrid.esgf-west.org/search/cmip6/ (see Table 1 for more details). Last accessed on 20 March 2026.

Author contributions

SSin analysed the data, prepared the figures and wrote the first version of the manuscript. SSaf and CC provided scientific support and supervised the study. SSaf generated the IASI Tskin product. JHL reconstructed the CO profiles from the EUMETSAT IASI CO CDR orbital files. SW and LC generated the IASI Cloud Detection Product. MDB generated the IASI CO CDR data. All authors contributed to the discussion and improvement of the manuscript.

Competing interests

The authors declare no conflicts of interest relevant to this study.

Acknowledgements

IASI is a joint mission of EUMETSAT and the Centre National d'Etudes Spatiales (CNES, France). We acknowledge the CNES for the financial support, the AERIS data infrastructure for providing access to the IASI data and ULB-LATMOS for the development of the retrieval algorithms. Activities at ULB have been supported by the HIRS Prodex arrangement (ESA-BELSPO). LC is Senior Research Associate supported by the Belgian F.R.S.-FNRS. We thank EUMETSAT through the Satellite Application Facility on Atmospheric Composition Monitoring (ACSAF) for the distribution of the IASI-CO product. We thank NASA's Goddard Earth Sciences Data and Information Services Center (GES DISC) for distributing the OMI Aura

https://doi.org/10.5194/egusphere-2026-4393
Preprint. Discussion started: 17 August 2026

data and the MERRA-2 reanalysis. We thank ECCAD for distributing the CAMS-GLOB-ANT emissions and CAMS Atmosphere Data Store for the GFAS emissions. We thank the CMIP6 project team for providing model outputs and CERES team for producing and providing the EBAF dataset.

References

Abeed, R., Viatte, C., Porter, W. C., Evangeliou, N., Clerbaux, C., Clarisse, L., Van Damme, M., Coheur, P.-F., and Safieddine, S.: A roadmap to estimating agricultural ammonia volatilization over Europe using satellite observations and simulation data, Atmospheric Chemistry and Physics, 23, 12505–12523, https://doi.org/10.5194/acp-23-12505-2023, 2023.

AC SAF: IASI Carbon Monoxide Profiles FORLI-CO Climate Data Record Release 1 - Metop-A and -B, https://doi.org/10.15770/EUM_SAF_AC_0047, 2024.

Albrecht, B. A.: Aerosols, Cloud Microphysics, and Fractional Cloudiness, Science, 245, 1227–1230, https://doi.org/10.1126/science.245.4923.1227, 1989.

Ali, Md. A., Assiri, M. E., Islam, M. N., Bilal, M., Ghulam, A., and Huang, Z.: Identification of NO2 and SO2 over China: Characterization of polluted and hotspots Provinces, Air Qual Atmos Health, 17, 2203–2221, https://doi.org/10.1007/s11869-024-01565-8, 2024.

Ambika, A. K. and Mishra, V.: Observational Evidence of Irrigation Influence on Vegetation Health and Land Surface Temperature in India, Geophysical Research Letters, 46, 13441–13451, https://doi.org/10.1029/2019GL084367, 2019.

Archibald, A. T., O'Connor, F. M., Abraham, N. L., Archer-Nicholls, S., Chipperfield, M. P., Dalvi, M., Folberth, G. A., Dennison, F., Dhomse, S. S., Griffiths, P. T., Hardacre, C., Hewitt, A. J., Hill, R. S., Johnson, C. E., Keeble, J., Köhler, M. O., Morgenstern, O., Mulcahy, J. P., Ordóñez, C., Pope, R. J., Rumbold, S. T., Russo, M. R., Savage, N. H., Sellar, A., Stringer, M., Turnock, S. T., Wild, O., and Zeng, G.: Description and evaluation of the UKCA stratosphere–troposphere chemistry scheme (StratTrop vn 1.0) implemented in UKESM1, Geoscientific Model Development, 13, 1223–1266, https://doi.org/10.5194/gmd-13-1223-2020, 2020.

Banks, A., Kooperman, G. J., and Xu, Y.: Meteorological Influences on Anthropogenic PM2.5 in Future Climates: Species Level Analysis in the Community Earth System Model v2, Earth's Future, 10, e2021EF002298, https://doi.org/10.1029/2021EF002298, 2022.

Bauduin, S., Clarisse, L., Theunissen, M., George, M., Hurtmans, D., Clerbaux, C., and Coheur, P.-F.: IASI's sensitivity to near-surface carbon monoxide (CO): Theoretical analyses and retrievals on test cases, Journal of Quantitative Spectroscopy and Radiative Transfer, 189, 428–440, https://doi.org/10.1016/j.jqsrt.2016.12.022, 2017.

Boersma, K. F., Eskes, H. J., and Brinksma, E. J.: Error analysis for tropospheric NO_2 retrieval from space, J. Geophys. Res., 109, 2003JD003962, https://doi.org/10.1029/2003JD003962, 2004.

Boynard, A., Clerbaux, C., Clarisse, L., Safieddine, S., Pommier, M., Van Damme, M., Bauduin, S., Oudot, C., Hadji-Lazaro, J., Hurtmans, D., and Coheur, P.-F.: First simultaneous space measurements of atmospheric pollutants in the boundary layer from IASI: A case study in the North China Plain, Geophysical Research Letters, 41, 645–651, https://doi.org/10.1002/2013GL058333, 2014.

Buchholz, R. R., Worden, H. M., Park, M., Francis, G., Deeter, M. N., Edwards, D. P., Emmons, L. K., Gaubert, B., Gille, J., Martínez-Alonso, S., Tang, W., Kumar, R., Drummond, J. R., Clerbaux, C., George, M., Coheur, P.-F., Hurtmans, D., Bowman, K. W., Luo, M., Payne, V. H., Worden, J. R., Chin, M., Levy, R. C., Warner, J., Wei, Z., and Kulawik, S. S.: Air pollution trends measured from Terra: CO and AOD over industrial, fire-prone, and background regions, Remote Sensing of Environment, 256, 112275, https://doi.org/10.1016/j.rse.2020.112275, 2021.

Bucsela, E. J., Krotkov, N. A., Celarier, E. A., Lamsal, L. N., Swartz, W. H., Bhartia, P. K., Boersma, K. F., Veefkind, J. P., Gleason, J. F., and Pickering, K. E.: A new stratospheric and tropospheric NO_2 retrieval algorithm for nadir-viewing satellite instruments: applications to OMI, Atmospheric Measurement Techniques, 6, 2607–2626, https://doi.org/10.5194/amt-6-2607-2013, 2013.

Chen, C., Park, T., Wang, X., Piao, S., Xu, B., Chaturvedi, R. K., Fuchs, R., Brovkin, V., Ciais, P., Fensholt, R., Tømmervik, H., Bala, G., Zhu, Z., Nemani, R. R., and Myneni, R. B.: China and India lead in greening of the world through land-use management, Nat Sustain, 2, 122–129, https://doi.org/10.1038/s41893-019-0220-7, 2019.

Chen, D., Ding, M., Sun, Q., and Zuo, T.: Aerosols modulate East Asian surface temperature: unique cloud-radiation feedback and species-dependent effects, npj Clean Air, 1, 36, https://doi.org/10.1038/s44407-025-00040-7, 2025a.

Chen, T.-M., Kuschner, W. G., Gokhale, J., and Shofer, S.: Outdoor Air Pollution: Nitrogen Dioxide, Sulfur Dioxide, and Carbon Monoxide Health Effects, The American Journal of the Medical Sciences, 333, 249–256, https://doi.org/10.1097/MAJ.0b013e31803b900f, 2007.

Chen, Y., van der A, R. J., Ding, J., Eskes, H., Williams, J. E., Theys, N., Tsikerdekis, A., and Levelt, P. F.: SO_2 emissions derived from TROPOMI observations over India using a flux-divergence method with variable lifetimes, Atmospheric Chemistry and Physics, 25, 1851–1868, https://doi.org/10.5194/acp-25-1851-2025, 2025b.

Chen, Z., Zhou, Z., Ji, C., Yao, Z., Mao, J., Wang, Z., Xiang, Y., Zhang, T., Zhou, Y., Chen, Z., and Dou, G.: Comparison of the polluted dust plume and natural dust air mass in a spring dust event in Beijing 2023, Journal of Environmental Sciences, 154, 760–773, https://doi.org/10.1016/j.jes.2024.07.003, 2025c.

Choi, M., Lim, H., Kim, J., Lee, S., Eck, T. F., Holben, B. N., Garay, M. J., Hyer, E. J., Saide, P. E., and Liu, H.: Validation, comparison, and integration of GOCI, AHI, MODIS, MISR, and VIIRS aerosol optical depth over East Asia during the 2016 KORUS-AQ campaign, Atmospheric Measurement Techniques, 12, 4619–4641, https://doi.org/10.5194/amt-12-4619-2019, 2019.

Clarisse, L., Fromm, M., Ngadi, Y., Emmons, L., Clerbaux, C., Hurtmans, D., and Coheur, P.-F.: Intercontinental transport of anthropogenic sulfur dioxide and other pollutants: An infrared remote sensing case study, Geophysical Research Letters, 38, https://doi.org/10.1029/2011GL048976, 2011.

Clerbaux, C., Boynard, A., Clarisse, L., George, M., Hadji-Lazaro, J., Herbin, H., Hurtmans, D., Pommier, M., Razavi, A., Turquety, S., Wespes, C., and Coheur, P.-F.: Monitoring of atmospheric composition using the thermal infrared IASI/MetOp sounder, Atmospheric Chemistry and Physics, 9, 6041–6054, https://doi.org/10.5194/acp-9-6041-2009, 2009.

Collins, W. J., Lamarque, J.-F., Schulz, M., Boucher, O., Eyring, V., Hegglin, M. I., Maycock, A., Myhre, G., Prather, M., Shindell, D., and Smith, S. J.: AerChemMIP: quantifying the effects of chemistry and aerosols in CMIP6, Geoscientific Model Development, 10, 585–607, https://doi.org/10.5194/gmd-10-585-2017, 2017.

Crippa, M., Guizzardi, D., Muntean, M., Schaaf, E., Dentener, F., Van Aardenne, J. A., Monni, S., Doering, U., Olivier, J. G. J., Pagliari, V., and Janssens-Maenhout, G.: Gridded emissions of air pollutants for the period 1970–2012 within EDGAR v4.3.2, Earth Syst. Sci. Data, 10, 1987–2013, https://doi.org/10.5194/essd-10-1987-2018, 2018.

https://doi.org/10.5194/egusphere-2026-4393
Preprint. Discussion started: 17 August 2026

Crippa, M., Guizzardi, D., Pisoni, E., Solazzo, E., Guion, A., Muntean, M., Florczyk, A., Schiavina, M., Melchiorri, M., and Hutfilter, A. F.: Global anthropogenic emissions in urban areas: patterns, trends, and challenges, Environ. Res. Lett., 16, 074033, https://doi.org/10.1088/1748-9326/ac00e2, 2021.

Cui, P., Jin, Y., Feng, H., Li, Z., Ding, S., and Li, Y.: Burden of carbon monoxide poisoning in China, 1990–2019: A systematic analysis of data from the global burden of disease study 2019, Front Public Health, 10, 930784, https://doi.org/10.3389/fpubh.2022.930784, 2022.

De Leeuw, G., van der A, R., Bai, J., den Hoed, M., Ding, J., Guo, J., Li, Z., Zhang, Y., Fan, C., Qin, K., Sinnathamby, S., Safieddine, S., Varotsos, C., Xue, Y., Yin, Y., Zhang, Q., Zhang, X., Zhang, X., and Zhang, X.: Remote sensing of air pollutants in China to study the effects of emission reduction policies on air quality, Journal of Atmospheric and Solar-Terrestrial Physics, 265, 106392, https://doi.org/10.1016/j.jastp.2024.106392, 2024.

Denier van der Gon, H., Gauss, M., Granier, C., Guevara, M., Arellano, S., Sindelarova, K., Liaskoni, M., Markova, J., Prieto Perez, A., Bartik, L., Jalkanen, J.-P., Majamäki, E., Quack, B., Bouarar, I., Li, C., Liousse, C., Simpson, D., Olivié, D., Benedictow, A., Segers, A., Zilbermann, N., Dellaert, S., Kuenen, J., Schoenmakers, E., Super, I., and Krueger, K.: Documentation of CAMS emission inventory products, https://doi.org/10.24380/UAG-0SVT, 2025.

Didan, K.: MODIS/Terra Vegetation Indices Monthly L3 Global 1km SIN Grid V061, https://doi.org/10.5067/MODIS/MOD13A3.061, 2021.

Doherty, R. M., O'Connor, F. M., and Turnock, S. T.: Projections of Future Air Quality Are Uncertain. But Which Source of Uncertainty Is Most Important?, JGR Atmospheres, 127, e2022JD037948, https://doi.org/10.1029/2022JD037948, 2022.

Dunne, J. P., Horowitz, L. W., Adcroft, A. J., Ginoux, P., Held, I. M., John, J. G., Krasting, J. P., Malyshev, S., Naik, V., Paulot, F., Shevliakova, E., Stock, C. A., Zadeh, N., Balaji, V., Blanton, C., Dunne, K. A., Dupuis, C., Durachta, J., Dussin, R., Gauthier, P. P. G., Griffies, S. M., Guo, H., Hallberg, R. W., Harrison, M., He, J., Hurlin, W., McHugh, C., Menzel, R., Milly, P. C. D., Nikonov, S., Paynter, D. J., Ploshay, J., Radhakrishnan, A., Rand, K., Reichl, B. G., Robinson, T., Schwarzkopf, D. M., Sentman, L. T., Underwood, S., Vahlenkamp, H., Winton, M., Wittenberg, A. T., Wyman, B., Zeng, Y., and Zhao, M.: The GFDL Earth System Model Version 4.1 (GFDL-ESM 4.1): Overall Coupled Model Description and Simulation Characteristics, Journal of Advances in Modeling Earth Systems, 12, e2019MS002015, https://doi.org/10.1029/2019MS002015, 2020.

Dunne, J. P., Hewitt, H. T., Arblaster, J. M., Bonou, F., Boucher, O., Cavazos, T., Dingley, B., Durack, P. J., Hassler, B., Juckes, M., Miyakawa, T., Mizielinski, M., Naik, V., Nicholls, Z., O'Rourke, E., Pincus, R., Sanderson, B. M., Simpson, I. R., and Taylor, K. E.: An evolving Coupled Model Intercomparison Project phase 7 (CMIP7) and Fast Track in support of future climate assessment, Geoscientific Model Development, 18, 6671–6700, https://doi.org/10.5194/gmd-18-6671-2025, 2025.

Ehret, A., Turquety, S., George, M., Hadji-Lazaro, J., and Clerbaux, C.: Increase in carbon monoxide (CO) and aerosol optical depth (AOD) observed by satellites in the Northern Hemisphere over the summers of 2008–2023, linked to an increase in wildfires, Atmospheric Chemistry and Physics, 25, 6365–6394, https://doi.org/10.5194/acp-25-6365-2025, 2025.

EUMETSAT: IASI Level 1C Climate Data Record Release 2 - Metop-A and -B (2), https://doi.org/10.15770/EUM_SEC_CLM_0064, 2025.

Eyring, V., Bony, S., Meehl, G. A., Senior, C. A., Stevens, B., Stouffer, R. J., and Taylor, K. E.: Overview of the Coupled Model Intercomparison Project Phase 6 (CMIP6) experimental design and organization, Geoscientific Model Development, 9, 1937–1958, https://doi.org/10.5194/gmd-9-1937-2016, 2016.

https://doi.org/10.5194/egusphere-2026-4393
Preprint. Discussion started: 17 August 2026

Fan, X., Zhen, X., Sun, X., Zheng, M., Zhang, T., He, W., and Han, C.: The Trends in Aerosol Optical Depth Over Eastern Asia Using Modis Measurements from 2001 to 2022, in: IGARSS 2025 - 2025 IEEE International Geoscience and Remote Sensing Symposium, IGARSS 2025 - 2025 IEEE International Geoscience and Remote Sensing Symposium, 3077–3081, https://doi.org/10.1109/IGARSS55030.2025.11242637, 2025.

Fioletov, V. E., McLinden, C. A., Griffin, D., Abboud, I., Krotkov, N., Leonard, P. J. T., Li, C., Joiner, J., Theys, N., and Carn, S.: Version 2 of the global catalogue of large anthropogenic and volcanic SO_2 sources and emissions derived from satellite measurements, Earth System Science Data, 15, 75–93, https://doi.org/10.5194/essd-15-75-2023, 2023.

Fitzenberger, B.: The moving blocks bootstrap and robust inference for linear least squares and quantile regressions, Journal of Econometrics, 82, 235–287, https://doi.org/10.1016/S0304-4076(97)00058-4, 1998.

Forster, P., Storelvmo, T., Armour, K., Collins, W., Dufresne, J.-L., Frame, D., Lunt, D. J., Mauritsen, T., Palmer, M. D., Watanabe, M., Wild, M., and Zhang, H.: The Earth's Energy Budget, Climate Feedbacks, and Climate Sensitivity, in: Climate Change 2021: The Physical Science Basis. Contribution of Working Group I to the Sixth Assessment Report of the Intergovernmental Panel on Climate Change, edited by: Masson-Delmotte, V., Zhai, P., Pirani, A., Connors, S. L., Péan, C., Berger, S., Caud, N., Chen, Y., Goldfarb, L., Gomis, M. I., Huang, M., Leitzell, K., Lonnoy, E., Matthews, J. B. R., Maycock, T. K., Waterfield, T., Yelekçi, O., Yu, R., and Zhou, B., Cambridge University Press, Cambridge, United Kingdom and New York, NY, USA, 923–1054, https://doi.org/10.1017/9781009157896.009, 2021.

Forster, P. M., Walsh, T., Smith, C., Lamb, W. F., Lamboll, R., Cassou, C., Hauser, M., Hausfather, Z., Lee, J.-Y., Palmer, M. D., Von Schuckmann, K., Slangen, A. B. A., Szopa, S., Trewin, B., Yun, J., P. Gillett, N., Jenkins, S., Matthews, H. D., Raghavan, K., Ribes, A., Rogelj, J., Rosen, D., Zhang, X., Allen, M., M. Andrew, R., Atkinson, C., Betts, R. A., Bombelli, A., Burgess, S. N., Cheng, L., Claxton, H. E., Friedlingstein, P., Frölicher, T. L., Domingues, C. M., Gasser, T., Gregory, C. H., Hoesly, R. M., Huppmann, D., Ishii, M., Kadow, C., Karwat, A., Kennedy, J., Killick, R. E., Kovilakam, M. V. M., Krummel, P. B., Lan, X., Lamarque, J.-F., Liné, A., Martín-Míguez, B., Monselesan, D. P., Morice, C., Mühle, J., Mussak, P., Peters, G. P., Pirani, A., Pongratz, J., Rigby, M., Rohde, R., Savita, A., Seneviratne, S. I., Smith, S. J., Taha, G., Tassone, C., Thorne, P., Wells, C., Western, L. M., Van Der Werf, G. R., Wijffels, S. E., Zecchetto, M., Zhong, J., Zhang, X., Masson-Delmotte, V., and Zhai, P.: Indicators of Global Climate Change 2025: annual update of key indicators of the state of the climate system and human influence, https://doi.org/10.5194/essd-2026-287, 23 April 2026.

Gelaro, R., McCarty, W., Suárez, M. J., Todling, R., Molod, A., Takacs, L., Randles, C. A., Darmenov, A., Bosilovich, M. G., Reichle, R., Wargan, K., Coy, L., Cullather, R., Draper, C., Akella, S., Buchard, V., Conaty, A., Silva, A. M. da, Gu, W., Kim, G.-K., Koster, R., Lucchesi, R., Merkova, D., Nielsen, J. E., Partyka, G., Pawson, S., Putman, W., Rienecker, M., Schubert, S. D., Sienkiewicz, M., and Zhao, B.: The Modern-Era Retrospective Analysis for Research and Applications, Version 2 (MERRA-2), Journal of Climate, 30, 5419–5454, https://doi.org/10.1175/JCLI-D-16-0758.1, 2017.

George, M., Clerbaux, C., Bouarar, I., Coheur, P.-F., Deeter, M. N., Edwards, D. P., Francis, G., Gille, J. C., Hadji-Lazaro, J., Hurtmans, D., Inness, A., Mao, D., and Worden, H. M.: An examination of the long-term CO records from MOPITT and IASI: comparison of retrieval methodology, Atmospheric Measurement Techniques, 8, 4313–4328, https://doi.org/10.5194/amt-8-4313-2015, 2015.

Gidden, M. J., Riahi, K., Smith, S. J., Fujimori, S., Luderer, G., Kriegler, E., van Vuuren, D. P., van den Berg, M., Feng, L., Klein, D., Calvin, K., Doelman, J. C., Frank, S., Fricko, O., Harmsen, M., Hasegawa, T., Havlik, P., Hilaire, J., Hoesly, R., Horing, J., Popp, A., Stehfest, E., and Takahashi, K.: Global emissions pathways under different socioeconomic scenarios for use in CMIP6: a dataset of harmonized emissions trajectories through the end of the century, Geoscientific Model Development, 12, 1443–1475, https://doi.org/10.5194/gmd-12-1443-2019, 2019.

Global Modeling And Assimilation Office: MERRA-2 tavg1_2d_rad_Nx: 2d,1-Hourly,Time-Averaged,Single-Level,Assimilation,Radiation Diagnostics V5.12.4, https://doi.org/10.5067/Q9QMY5PBNV1T, 2015a.

https://doi.org/10.5194/egusphere-2026-4393
Preprint. Discussion started: 17 August 2026

Global Modeling And Assimilation Office: MERRA-2 tavg1_2d_slv_Nx: 2d,1-Hourly,Time-Averaged,Single-Level,Assimilation,Single-Level Diagnostics V5.12.4, https://doi.org/10.5067/VJAFPLI1CSIV, 2015b.

Gomez, J., Allen, R. J., Turnock, S. T., Horowitz, L. W., Tsigaridis, K., Bauer, S. E., Olivié, D., Thomson, E. S., and Ginoux, P.: The projected future degradation in air quality is caused by more abundant natural aerosols in a warmer world, Commun Earth Environ, 4, 22, https://doi.org/10.1038/s43247-023-00688-7, 2023.

Good, P., Sellar, A., Tang, Y., Rumbold, S., Ellis, R., Kelley, D., Kuhlbrodt, T., and Walton, J.: MOHC UKESM1.0-LL model output prepared for CMIP6 ScenarioMIP (20250528), https://doi.org/10.22033/ESGF/CMIP6.1567, 2019.

Gulia, S., Shukla, N., Padhi, L., Bosu, P., Goyal, S. K., and Kumar, R.: Evolution of air pollution management policies and related research in India, Environmental Challenges, 6, 100431, https://doi.org/10.1016/j.envc.2021.100431, 2022.

Guttikunda, S. K., Dammalapati, S. K., and Pradhan, G.: Assessing air quality during India's National Clean Air Programme (NCAP): 2019–2023, Atmospheric Environment, 343, 120974, https://doi.org/10.1016/j.atmosenv.2024.120974, 2025.

Hampel, F. R.: The Influence Curve and its Role in Robust Estimation, Journal of the American Statistical Association, 69, 383–393, https://doi.org/10.1080/01621459.1974.10482962, 1974.

Hoesly, R. M., Smith, S. J., Feng, L., Klimont, Z., Janssens-Maenhout, G., Pitkanen, T., Seibert, J. J., Vu, L., Andres, R. J., Bolt, R. M., Bond, T. C., Dawidowski, L., Kholod, N., Kurokawa, J., Li, M., Liu, L., Lu, Z., Moura, M. C. P., O'Rourke, P. R., and Zhang, Q.: Historical (1750–2014) anthropogenic emissions of reactive gases and aerosols from the Community Emissions Data System (CEDS), Geoscientific Model Development, 11, 369–408, https://doi.org/10.5194/gmd-11-369-2018, 2018.

Holloway, T., Levy II, H., and Kasibhatla, P.: Global distribution of carbon monoxide, Journal of Geophysical Research: Atmospheres, 105, 12123–12147, https://doi.org/10.1029/1999JD901173, 2000.

Horowitz, L. W., Naik, V., Paulot, F., Ginoux, P. A., Dunne, J. P., Mao, J., Schnell, J., Chen, X., He, J., John, J. G., Lin, M., Lin, P., Malyshev, S., Paynter, D., Shevliakova, E., and Zhao, M.: The GFDL Global Atmospheric Chemistry-Climate Model AM4.1: Model Description and Simulation Characteristics, J Adv Model Earth Syst, 12, e2019MS002032, https://doi.org/10.1029/2019MS002032, 2020.

Huang, Y., Dickinson, R. E., and Chameides, W. L.: Impact of aerosol indirect effect on surface temperature over East Asia, Proc. Natl. Acad. Sci. U.S.A., 103, 4371–4376, https://doi.org/10.1073/pnas.0504428103, 2006.

Hurtmans, D., Coheur, P.-F., Wespes, C., Clarisse, L., Scharf, O., Clerbaux, C., Hadji-Lazaro, J., George, M., and Turquety, S.: FORLI radiative transfer and retrieval code for IASI, Journal of Quantitative Spectroscopy and Radiative Transfer, 113, 1391–1408, https://doi.org/10.1016/j.jqsrt.2012.02.036, 2012.

Ikeda, K., Tanimoto, H., Kanaya, Y., Taketani, F., and Matsuki, A.: Evaluation of Black Carbon Concentration Levels and Trends in East Asia from CMIP6 Climate Models: Comparison to Long-Term Observations in Japan and Biases Due to Chinese Emissions, Sola, 19, 239–245, https://doi.org/10.2151/sola.2023-031, 2023.

Intergovernmental Panel On Climate Change (Ed.): Clouds and Aerosols, in: Climate Change 2013 – The Physical Science Basis, Cambridge University Press, 571–658, https://doi.org/10.1017/CBO9781107415324.016, 2014.

Intergovernmental Panel On Climate Change (IPCC): Climate Change 2023: Synthesis Report. Contribution of Working Groups I, II and III to the Sixth Assessment Report of the Intergovernmental Panel on Climate Change, Intergovernmental Panel on Climate Change (IPCC), https://doi.org/10.59327/IPCC/AR6-9789291691647, 2023.

Ismaeel, A., Tai, A. P. K., and Wu, J.: Understanding the spatial patterns of atmospheric ammonia trends in South Asia, Science of The Total Environment, 954, 176188, https://doi.org/10.1016/j.scitotenv.2024.176188, 2024.

Iturbide, M., Gutiérrez, J. M., Alves, L. M., Bedia, J., Cerezo-Mota, R., Cimadevilla, E., Cofiño, A. S., Di Luca, A., Faria, S. H., Gorodetskaya, I. V., Hauser, M., Herrera, S., Hennessy, K., Hewitt, H. T., Jones, R. G., Krakovska, S., Manzanas, R., Martínez-Castro, D., Narisma, G. T., Nurhati, I. S., Pinto, I., Seneviratne, S. I., van den Hurk, B., and Vera, C. S.: An update of IPCC climate reference regions for subcontinental analysis of climate model data: definition and aggregated datasets, Earth System Science Data, 12, 2959–2970, https://doi.org/10.5194/essd-12-2959-2020, 2020.

Jacob, D. J.: Introduction to Atmospheric Chemistry, Princeton University Press, https://doi.org/10.1515/9781400841547, 2000.

Jain, M., Saxena, P., and Sonwani, S.: Characteristics, dynamics, and impact of the Thar Desert dust storms on air quality over northern India, Nat Hazards, 121, 5589–5619, https://doi.org/10.1007/s11069-024-07003-3, 2025.

Jo, H., Kim, T. H., Park, J., Oh, J., Kim, M. S., Abid, S. U. A., Adhikary, R. K., Adnani, Q. E. S., Agrawal, A., Ahmad, D., Ahmad, K., Ahmad, S., Ahmad, T., Ahmed, A. M., Ahmed, H., Ahmed, M. F., Ahmed, N., Ahmed, S. A., Akkaif, M. A., Hasan, S. M. A., Alam, K., Ali, M. U., Ali, R., Ali, S. S., Ali, S. Y., Alif, S. M., Aljunid, S. M., Al-Mamun, M., Altaf, A., Annadurai, K., Ansari, S., Arockiaraj, J., Arooj, M., Aryntayeva, N., Asdaq, S. M. B., Ashraf, M. A. B., Ashraf, S. A., Ashraf, T., Asri, Y., Assariparambil, A. R., Babu, G. R., Badiye, A. D., Baig, A. A., Bakkannavar, S. M., Banik, B., Bardhan, M., Basu, S., Beeraka, N. M., Tune, S. N. B. K., Bhandari, J., Bhandari, N., Bhat, A. N., Bhat, A., Bhatnagar, A., Bhattacharjee, P., Biswas, B., Biswas, M. S., Bitar, A. N., Bui, L. P., Butt, N. S., Butt, Z. A., Cenderadewi, M., Chakraborty, C., Chakraborty, S., Chan, J. S. K., Chattu, V. K., Chaudhuri, S., Chen, A.-T., Chen, H., Chopra, H., Chu, D.-T., Chung, S., Devanbu, V. G. C., Devegowda, D., Dewan, S. M. R., Dhane, A. S., Dharmagadda, S., Dharmaratne, S. D., Dhital, N. B., Dhungel, B., Ding, G., Ding, X., Do, H. P., Do, T. H. P., Doshi, O. P., Dutta, S., Efendi, F., Elsohaby, I., Fahim, A., Fakhradiyev, I. R., Fareed, M., Fatima, Z., Fekadu, G., G, S., Ganesh, B., Gao, X., Gautam, R. K., Ghuge, A., Gil, A. U., et al.: Burden of chronic respiratory disease in Asia, 1990–2023: a systematic analysis for the Global Burden of Disease Study 2023, The Lancet Respiratory Medicine, 14, 233–255, https://doi.org/10.1016/S2213-2600(25)00404-7, 2026.

John, J. G., Blanton, C., McHugh, C., Radhakrishnan, A., Rand, K., Vahlenkamp, H., Wilson, C., Zadeh, N. T., Dunne, J. P., Dussin, R., Horowitz, L. W., Krasting, J. P., Lin, P., Malyshev, S., Naik, V., Ploshay, J., Shevliakova, E., Silvers, L., Stock, C., Winton, M., and Zeng, Y.: NOAA-GFDL GFDL-ESM4 model output prepared for CMIP6 ScenarioMIP (20250528), https://doi.org/10.22033/ESGF/CMIP6.1414, 2018.

Kaiser, J. W., Heil, A., Andreae, M. O., Benedetti, A., Chubarova, N., Jones, L., Morcrette, J.-J., Razinger, M., Schultz, M. G., Suttie, M., and van der Werf, G. R.: Biomass burning emissions estimated with a global fire assimilation system based on observed fire radiative power, Biogeosciences, 9, 527–554, https://doi.org/10.5194/bg-9-527-2012, 2012.

Kalisoras, A., Georgoulias, A. K., Akritidis, D., Allen, R. J., Naik, V., Kuo, C., Szopa, S., Nabat, P., Olivié, D., van Noije, T., Le Sager, P., Neubauer, D., Oshima, N., Mulcahy, J., Horowitz, L. W., and Zanis, P.: Decomposing the effective radiative forcing of anthropogenic aerosols based on CMIP6 Earth system models, Atmospheric Chemistry and Physics, 24, 7837–7872, https://doi.org/10.5194/acp-24-7837-2024, 2024.

Kant, Y., Chauhan, P., Natwariya, A., Kannaujiya, S., and Mitra, D.: Long term influence of groundwater preservation policy on stubble burning and air pollution over North-West India, Sci Rep, 12, 2090, https://doi.org/10.1038/s41598-022-06043-8, 2022.

Kato, S., Rose, F. G., Rutan, D. A., Thorsen, T. J., Loeb, N. G., Doelling, D. R., Huang, X., Smith, W. L., Su, W., and Ham, S.-H.: Surface Irradiances of Edition 4.0 Clouds and the Earth's Radiant Energy System (CERES) Energy Balanced and Filled (EBAF) Data Product, Journal of Climate, 31, 4501–4527, https://doi.org/10.1175/JCLI-D-17-0523.1, 2018.

https://doi.org/10.5194/egusphere-2026-4393
Preprint. Discussion started: 17 August 2026

Kato, S., Loeb, N. G., Rose, F. G., Ham, S.-H., Thorsen, T. J., Rutan, D. A., Miller, W. F., Caldwell, T. E., Doelling, D. R., and Sun-Mack, S.: Seamless Continuity in CERES Energy Balanced and Filled (EBAF) Surface Radiation Budget across Multiple Satellites, Journal of Climate, 38, 2461–2478, https://doi.org/10.1175/JCLI-D-23-0568.1, 2025.

Katzenberger, A., Schewe, J., Pongratz, J., and Levermann, A.: Robust increase of Indian monsoon rainfall and its variability under future warming in CMIP6 models, Earth System Dynamics, 12, 367–386, https://doi.org/10.5194/esd-12-367-2021, 2021.

Koenker, R. and Bassett, G.: Regression Quantiles, Econometrica, 46, 33–50, https://doi.org/10.2307/1913643, 1978.

Krasting, J. P., John, J. G., Blanton, C., McHugh, C., Nikonov, S., Radhakrishnan, A., Rand, K., Zadeh, N. T., Balaji, V., Durachta, J., Dupuis, C., Menzel, R., Robinson, T., Underwood, S., Vahlenkamp, H., Dunne, K. A., Gauthier, P. P., Ginoux, P., Griffies, S. M., Hallberg, R., Harrison, M., Hurlin, W., Malyshev, S., Naik, V., Paulot, F., Paynter, D. J., Ploshay, J., Reichl, B. G., Schwarzkopf, D. M., Seman, C. J., Silvers, L., Wyman, B., Zeng, Y., Adcroft, A., Dunne, J. P., Dussin, R., Guo, H., He, J., Held, I. M., Horowitz, L. W., Lin, P., Milly, P. C. D., Shevliakova, E., Stock, C., Winton, M., Wittenberg, A. T., Xie, Y., and Zhao, M.: NOAA-GFDL GFDL-ESM4 model output prepared for CMIP6 CMIP historical (20250528), https://doi.org/10.22033/ESGF/CMIP6.8597, 2018.

Krishnan, R. and Ramanathan, V.: Evidence of surface cooling from absorbing aerosols, Geophysical Research Letters, 29, https://doi.org/10.1029/2002GL014687, 2002.

Krotkov, N. A. and Can, L.: README Document for OMSO2: Aura/OMI Sulfur Dioxide Level 2 Product, NASA Goddard Space Flight Center, Greenbelt, MD 20771 USA, 2025.

Krotkov, N. A. and Li, C.: OMI/Aura Sulphur Dioxide (SO2) Total Column 1-orbit L2 Swath 13x24 km, https://doi.org/10.5067/AURA/OMI/DATA2422, 2025.

Krotkov, N. A., McLinden, C. A., Li, C., Lamsal, L. N., Celarier, E. A., Marchenko, S. V., Swartz, W. H., Bucsela, E. J., Joiner, J., Duncan, B. N., Boersma, K. F., Veefkind, J. P., Levelt, P. F., Fioletov, V. E., Dickerson, R. R., He, H., Lu, Z., and Streets, D. G.: Aura OMI observations of regional SO_2 and NO_2 pollution changes from 2005 to 2015, Atmospheric Chemistry and Physics, 16, 4605–4629, https://doi.org/10.5194/acp-16-4605-2016, 2016.

Krotkov, N. A., Lamsal, L. N., Marchenko, S. V., Fisher, B. L., Bucsela, E. J., Fasnacht, Z., Yang, E.-S., Qin, W., Vasilkov, A. V., Li, C., Joiner, J., Sunny, C., and Swartz, W. H.: OMI/Aura Nitrogen Dioxide (NO2) Total and Tropospheric Column 1-orbit L2 Swath 13x24 km, https://doi.org/10.5067/AURA/OMI/DATA2417, 2024a.

Krotkov, N. A., Lamsal, L. N., Marchenko, S., Fischer, B. L., and Bucsela, E. J.: OMNO2 README Document Data Product, Collection 4, Version 5.0, 2024b.

Kurokawa, J. and Ohara, T.: Long-term historical trends in air pollutant emissions in Asia: Regional Emission inventory in ASia (REAS) version 3, Atmospheric Chemistry and Physics, 20, 12761–12793, https://doi.org/10.5194/acp-20-12761-2020, 2020.

Kuttippurath, J. and Kashyap, R.: Greening of India: Forests or Croplands?, Applied Geography, 161, 103115, https://doi.org/10.1016/j.apgeog.2023.103115, 2023.

Lamsal, L. N., Krotkov, N. A., Vasilkov, A., Marchenko, S., Qin, W., Yang, E.-S., Fasnacht, Z., Joiner, J., Choi, S., Haffner, D., Swartz, W. H., Fisher, B., and Bucsela, E.: Ozone Monitoring Instrument (OMI) Aura nitrogen dioxide standard product version 4.0 with improved surface and cloud treatments, Atmospheric Measurement Techniques, 14, 455–479, https://doi.org/10.5194/amt-14-455-2021, 2021.

https://doi.org/10.5194/egusphere-2026-4393
Preprint. Discussion started: 17 August 2026

Lange, K., Richter, A., and Burrows, J. P.: Variability of nitrogen oxide emission fluxes and lifetimes estimated from Sentinel-5P TROPOMI observations, Atmos. Chem. Phys., 22, 2745–2767, https://doi.org/10.5194/acp-22-2745-2022, 2022.

Lee, C., Martin, R. V., Van Donkelaar, A., Lee, H., Dickerson, R. R., Hains, J. C., Krotkov, N., Richter, A., Vinnikov, K., and Schwab, J. J.: SO_2 emissions and lifetimes: Estimates from inverse modeling using in situ and global, space-based (SCIAMACHY and OMI) observations, J. Geophys. Res., 116, D06304, https://doi.org/10.1029/2010JD014758, 2011.

Lelieveld, J., Crutzen, P. J., Ramanathan, V., Andreae, M. O., Brenninkmeijer, C. A. M., Campos, T., Cass, G. R., Dickerson, R. R., Fischer, H., de Gouw, J. A., Hansel, A., Jefferson, A., Kley, D., de Laat, A. T. J., Lal, S., Lawrence, M. G., Lobert, J. M., Mayol-Bracero, O. L., Mitra, A. P., Novakov, T., Oltmans, S. J., Prather, K. A., Reiner, T., Rodhe, H., Scheeren, H. A., Sikka, D., and Williams, J.: The Indian Ocean Experiment: Widespread Air Pollution from South and Southeast Asia, Science, 291, 1031–1036, https://doi.org/10.1126/science.1057103, 2001.

Levelt, P. F., van den Oord, G. H. J., Dobber, M. R., Malkki, A., Visser, H., Vries, J. de, Stammes, P., Lundell, J. O. V., and Saari, H.: The ozone monitoring instrument, IEEE Transactions on Geoscience and Remote Sensing, 44, 1093–1101, https://doi.org/10.1109/TGRS.2006.872333, 2006.

Li, C., McLinden, C., Fioletov, V., Krotkov, N., Carn, S., Joiner, J., Streets, D., He, H., Ren, X., Li, Z., and Dickerson, R. R.: India Is Overtaking China as the World's Largest Emitter of Anthropogenic Sulfur Dioxide, Sci Rep, 7, 14304, https://doi.org/10.1038/s41598-017-14639-8, 2017.

Li, C., Krotkov, N. A., Leonard, P. J. T., Carn, S., Joiner, J., Spurr, R. J. D., and Vasilkov, A.: Version 2 Ozone Monitoring Instrument SO_2 product (OMSO2 V2): new anthropogenic SO_2 vertical column density dataset, Atmospheric Measurement Techniques, 13, 6175–6191, https://doi.org/10.5194/amt-13-6175-2020, 2020.

Li, J., Miao, C., Wei, W., Zhang, G., Hua, L., Chen, Y., and Wang, X.: Evaluation of CMIP6 Global Climate Models for Simulating Land Surface Energy and Water Fluxes During 1979–2014, Journal of Advances in Modeling Earth Systems, 13, e2021MS002515, https://doi.org/10.1029/2021MS002515, 2021.

Li, Y., Zhao, M., Motesharrei, S., Mu, Q., Kalnay, E., and Li, S.: Local cooling and warming effects of forests based on satellite observations, Nat Commun, 6, 6603, https://doi.org/10.1038/ncomms7603, 2015.

Liu, H., Yu, Y., Xia, D., Zhao, S., Ma, X., and Dong, L.: Analysis of the relationship between dust aerosol and precipitation in spring over East Asia using EOF and SVD methods, Science of The Total Environment, 908, 168437, https://doi.org/10.1016/j.scitotenv.2023.168437, 2024.

Loeb, N. G., Doelling, D. R., Wang, H., Su, W., Nguyen, C., Corbett, J. G., Liang, L., Mitrescu, C., Rose, F. G., and Kato, S.: Clouds and the Earth's Radiant Energy System (CERES) Energy Balanced and Filled (EBAF) Top-of-Atmosphere (TOA) Edition-4.0 Data Product, Journal of Climate, 31, 895–918, https://doi.org/10.1175/JCLI-D-17-0208.1, 2018.

Loeb, N. G., Doelling, D. R., Kato, S., Su, W., Mlynczak, P. E., and Wilkins, J. C.: Continuity in Top-of-Atmosphere Earth Radiation Budget Observations, Journal of Climate, 37, 6093–6108, https://doi.org/10.1175/JCLI-D-24-0180.1, 2024.

Luo, F., Samset, B. H., Stjern, C. W., Joshi, M., Wilcox, L. J., Allen, R. J., Hua, W., and Li, S.: Physical processes influencing the Asian climate due to black carbon emission over East Asia and South Asia, Atmospheric Chemistry and Physics, 25, 7647–7667, https://doi.org/10.5194/acp-25-7647-2025, 2025.

Luo, X., Ge, J., Cao, Y., Liu, Y., Yang, L., Wang, S., and Guo, W.: Local and Nonlocal Biophysical Effects of Historical Land Use and Land Cover Changes in CMIP6 Models and the Intermodel Uncertainty, Earth's Future, 12, e2023EF004220, https://doi.org/10.1029/2023EF004220, 2024.

https://doi.org/10.5194/egusphere-2026-4393
Preprint. Discussion started: 17 August 2026

Meng, J., Gao, Y., Wang, Y., Sheng, L., and Zhang, S.: Evaluating the climate projections for China through the lens of the simulations of planetary boundary layer height, Atmospheric Research, 294, 106975, https://doi.org/10.1016/j.atmosres.2023.106975, 2023.

Ministry of Climate Change: National Clean Air Policy (NCAP), Ministry of Climate Change, Government of Pakistan, 2023.

Ministry of Environment, Forest, and Climate Change: Bangladesh National Air Quality Management Plan 2024-2030, Ministry of Environment, Forest, and Climate Change, Government of Bangladesh, 2024.

MODIS Atmosphere Science Team: MOD08_D3 MODIS/Terra Aerosol Cloud Water Vapor Ozone Daily L3 Global 1Deg CMG, https://doi.org/10.5067/MODIS/MOD08_D3.006, 2015.

Mulcahy, J. P., Jones, C., Sellar, A., Johnson, B., Boutle, I. A., Jones, A., Andrews, T., Rumbold, S. T., Mollard, J., Bellouin, N., Johnson, C. E., Williams, K. D., Grosvenor, D. P., and McCoy, D. T.: Improved Aerosol Processes and Effective Radiative Forcing in HadGEM3 and UKESM1, https://doi.org/10.1029/2018MS001464, 2018.

Niu, X., Tang, J., Wang, S., and Fu, C.: Impact of future land use and land cover change on temperature projections over East Asia, Clim Dyn, 52, 6475–6490, https://doi.org/10.1007/s00382-018-4525-4, 2019.

O'Neill, B. C., Tebaldi, C., van Vuuren, D. P., Eyring, V., Friedlingstein, P., Hurtt, G., Knutti, R., Kriegler, E., Lamarque, J.-F., Lowe, J., Meehl, G. A., Moss, R., Riahi, K., and Sanderson, B. M.: The Scenario Model Intercomparison Project (ScenarioMIP) for CMIP6, Geoscientific Model Development, 9, 3461–3482, https://doi.org/10.5194/gmd-9-3461-2016, 2016.

Oshima, N., Yukimoto, S., Deushi, M., Koshiro, T., Kawai, H., Tanaka, T. Y., and Yoshida, K.: Global and Arctic effective radiative forcing of anthropogenic gases and aerosols in MRI-ESM2.0, Prog Earth Planet Sci, 7, 38, https://doi.org/10.1186/s40645-020-00348-w, 2020.

Pandey, A. K., Stevenson, D. S., Zhao, A., Pope, R. J., Hossaini, R., Kumar, K., and Chipperfield, M. P.: Evaluating tropospheric nitrogen dioxide in UKCA using OMI satellite retrievals over south and east Asia, Atmospheric Chemistry and Physics, 25, 4785–4802, https://doi.org/10.5194/acp-25-4785-2025, 2025.

Pandey, S. K., Vinoj, V., Landu, K., and Babu, S. S.: Declining pre-monsoon dust loading over South Asia: Signature of a changing regional climate, Sci Rep, 7, 16062, https://doi.org/10.1038/s41598-017-16338-w, 2017.

Pathak, M. and Kuttippurath, J.: Drastic changes in carbon monoxide pollution in rural India (2000–2019) and its CMIP6 model future (2015–2100) projections, Chemosphere, 394, 144814, https://doi.org/10.1016/j.chemosphere.2025.144814, 2026.

Paulot, F., Naik, V., and W. Horowitz, L.: Reduction in Near-Surface Wind Speeds With Increasing CO2 May Worsen Winter Air Quality in the Indo-Gangetic Plain, Geophysical Research Letters, 49, e2022GL099039, https://doi.org/10.1029/2022GL099039, 2022.

Payra, S., Sharma, A., Mishra, M. K., and Verma, S.: Performance evaluation of MODIS and VIIRS satellite AOD products over the Indian subcontinent, Front. Environ. Sci., 11, https://doi.org/10.3389/fenvs.2023.1158641, 2023.

Peng, X., Fu, N., Wang, J., Chen, Y., Mao, K., Zhang, L., Qin, Y., Ye, J., Du, W., Zhang, P., Pan, B., and Tao, S.: The impact of China's Clean Air Action and future strategies: Actions targeting regionally dominant sources, Journal of Environmental Management, 394, 127680, https://doi.org/10.1016/j.jenvman.2025.127680, 2025.

Popp, A., Calvin, K., Fujimori, S., Havlik, P., Humpenöder, F., Stehfest, E., Bodirsky, B. L., Dietrich, J. P., Doelmann, J. C., Gusti, M., Hasegawa, T., Kyle, P., Obersteiner, M., Tabeau, A., Takahashi, K., Valin, H., Waldhoff, S., Weindl, I., Wise, M., Kriegler, E., Lotze-Campen, H., Fricko, O., Riahi, K., and Vuuren, D. P. van: Land-use futures in the shared socio-economic pathways, Global Environmental Change, 42, 331–345, https://doi.org/10.1016/j.gloenvcha.2016.10.002, 2017.

Prasad, A. K. and Singh, R. P.: Changes in aerosol parameters during major dust storm events (2001–2005) over the Indo-Gangetic Plains using AERONET and MODIS data, Journal of Geophysical Research: Atmospheres, 112, https://doi.org/10.1029/2006JD007778, 2007.

Rahman, M. M., Wang, S., Zhao, W., Arshad, A., Zhang, W., and He, C.: Comprehensive Evaluation of Spatial Distribution and Temporal Trend of NO2, SO2 and AOD Using Satellite Observations over South and East Asia from 2011 to 2021, Remote Sensing, 15, 5069, https://doi.org/10.3390/rs15205069, 2023.

Ramachandran, S., Rupakheti, M., and Cherian, R.: Insights into recent aerosol trends over Asia from observations and CMIP6 simulations, Science of The Total Environment, 807, 150756, https://doi.org/10.1016/j.scitotenv.2021.150756, 2022.

Rao, S., Klimont, Z., Smith, S. J., Van Dingenen, R., Dentener, F., Bouwman, L., Riahi, K., Amann, M., Bodirsky, B. L., van Vuuren, D. P., Aleluia Reis, L., Calvin, K., Drouet, L., Fricko, O., Fujimori, S., Gernaat, D., Havlik, P., Harmsen, M., Hasegawa, T., Heyes, C., Hilaire, J., Luderer, G., Masui, T., Stehfest, E., Strefler, J., van der Sluis, S., and Tavoni, M.: Future air pollution in the Shared Socio-economic Pathways, Global Environmental Change, 42, 346–358, https://doi.org/10.1016/j.gloenvcha.2016.05.012, 2017.

Reddy, C. S., Unnikrishnan, A., Bird, N. G., Faseela, V. S., Asra, M., Manikandan, T. M., and Rao, P. V. N.: Characterizing Vegetation Fire dynamics in Myanmar and South Asian Countries, J Indian Soc Remote Sens, 48, 1829–1843, https://doi.org/10.1007/s12524-020-01205-5, 2020.

Ren, F., Lin, J., Xu, C., Adeniran, J. A., Wang, J., Martin, R. V., van Donkelaar, A., Hammer, M. S., Horowitz, L. W., Turnock, S. T., Oshima, N., Zhang, J., Bauer, S., Tsigaridis, K., Seland, Ø., Nabat, P., Neubauer, D., Strand, G., van Noije, T., Le Sager, P., and Takemura, T.: Evaluation of CMIP6 model simulations of $PM_{2.5}$ and its components over China, Geoscientific Model Development, 17, 4821–4836, https://doi.org/10.5194/gmd-17-4821-2024, 2024.

Riahi, K., van Vuuren, D. P., Kriegler, E., Edmonds, J., O'Neill, B. C., Fujimori, S., Bauer, N., Calvin, K., Dellink, R., Fricko, O., Lutz, W., Popp, A., Cuaresma, J. C., Kc, S., Leimbach, M., Jiang, L., Kram, T., Rao, S., Emmerling, J., Ebi, K., Hasegawa, T., Havlik, P., Humpenöder, F., Da Silva, L. A., Smith, S., Stehfest, E., Bosetti, V., Eom, J., Gernaat, D., Masui, T., Rogelj, J., Strefler, J., Drouet, L., Krey, V., Luderer, G., Harmsen, M., Takahashi, K., Baumstark, L., Doelman, J. C., Kainuma, M., Klimont, Z., Marangoni, G., Lotze-Campen, H., Obersteiner, M., Tabeau, A., and Tavoni, M.: The Shared Socioeconomic Pathways and their energy, land use, and greenhouse gas emissions implications: An overview, Global Environmental Change, 42, 153–168, https://doi.org/10.1016/j.gloenvcha.2016.05.009, 2017.

Safieddine, S., Parracho, A. C., George, M., Aires, F., Pellet, V., Clarisse, L., Whitburn, S., Lezeaux, O., Thépaut, J.-N., Hersbach, H., Radnoti, G., Goettsche, F., Martin, M., Doutriaux-Boucher, M., Coppens, D., August, T., Zhou, D. K., and Clerbaux, C.: Artificial Neural Networks to Retrieve Land and Sea Skin Temperature from IASI, Remote Sensing, 12, https://doi.org/10.3390/rs12172777, 2020.

Safieddine, S., Clerbaux, C., Clarisse, L., Whitburn, S., and Eltahir, E. A. B.: Present and future land surface and wet bulb temperatures in the Arabian Peninsula, Environ. Res. Lett., 17, 044029, https://doi.org/10.1088/1748-9326/ac507c, 2022.

Safieddine, S., Clerbaux, C., Muñoz-Sabater, J., and Thépaut, J.-N.: Local hourly trends in near-surface and land surface temperatures, Sci Rep, 15, 29915, https://doi.org/10.1038/s41598-025-15731-0, 2025.

https://doi.org/10.5194/egusphere-2026-4393
Preprint. Discussion started: 17 August 2026

Safieddine, S., Sinnathamby, S., Hadji-Lazaro, J., Doutriaux-Boucher, M., Ghent, D., Whitburn, S., Clarisse, L., and Clerbaux, C.: Assessing Earth’s Skin Temperature Trends: Consistent Signals from IASI, MODIS, CCI and ERA5, EGUsphere, 1–21, https://doi.org/10.5194/egusphere-2026-400, 2026.

Samset, B. H., Lund, M. T., Bollasina, M., Myhre, G., and Wilcox, L.: Emerging Asian aerosol patterns, Nat. Geosci., 12, 582–584, https://doi.org/10.1038/s41561-019-0424-5, 2019.

Santer, B. D., Mears, C., Doutriaux, C., Caldwell, P., Gleckler, P. J., Wigley, T. M. L., Solomon, S., Gillett, N. P., Ivanova, D., Karl, T. R., Lanzante, J. R., Meehl, G. A., Stott, P. A., Taylor, K. E., Thorne, P. W., Wehner, M. F., and Wentz, F. J.: Separating signal and noise in atmospheric temperature changes: The importance of timescale, Journal of Geophysical Research: Atmospheres, 116, https://doi.org/10.1029/2011JD016263, 2011.

Sarangi, C., Kanawade, V. P., Tripathi, S. N., Thomas, A., and Ganguly, D.: Aerosol-induced intensification of cooling effect of clouds during Indian summer monsoon, Nat Commun, 9, 3754, https://doi.org/10.1038/s41467-018-06015-5, 2018.

Sarin, T. S. and Vinoj, V.: Assessing the relationship between atmospheric aerosols and maximum surface air temperature over the Indian region, Sci Rep, https://doi.org/10.1038/s41598-026-40641-0, 2026.

Seinfeld, J. H. and Pandis, S. N.: Atmospheric chemistry and physics: from air pollution to climate change, Third edition., John Wiley & Sons, Inc, Hoboken, New Jersey, 1120 pp., 2016.

Sellar, A. A., Jones, C. G., Mulcahy, J. P., Tang, Y., Yool, A., Wiltshire, A., O'Connor, F. M., Stringer, M., Hill, R., Palmieri, J., Woodward, S., de Mora, L., Kuhlbrodt, T., Rumbold, S. T., Kelley, D. I., Ellis, R., Johnson, C. E., Walton, J., Abraham, N. L., Andrews, M. B., Andrews, T., Archibald, A. T., Berthou, S., Burke, E., Blockley, E., Carslaw, K., Dalvi, M., Edwards, J., Folberth, G. A., Gedney, N., Griffiths, P. T., Harper, A. B., Hendry, M. A., Hewitt, A. J., Johnson, B., Jones, A., Jones, C. D., Keeble, J., Liddicoat, S., Morgenstern, O., Parker, R. J., Predoi, V., Robertson, E., Siahaan, A., Smith, R. S., Swaminathan, R., Woodhouse, M. T., Zeng, G., and Zerroukat, M.: UKESM1: Description and Evaluation of the U.K. Earth System Model, Journal of Advances in Modeling Earth Systems, 11, 4513–4558, https://doi.org/10.1029/2019MS001739, 2019.

Shin, H. H., Ming, Y., Zhao, M., Golaz, J.-C., Xiang, B., and Guo, H.: Evaluation of Planetary Boundary Layer Simulation in GFDL Atmospheric General Circulation Models, Journal of Climate, 31, 5071–5087, https://doi.org/10.1175/JCLI-D-17-0543.1, 2018.

Sinnathamby, S., Safieddine, S., Doutriaux-Boucher, M., Coheur, P., and Clerbaux, C.: Post-Monsoon Pollution Events in the Indo-Gangetic Plain Using 18 Years [2007–2024] of IASI Carbon Monoxide Satellite Measurements, Journal of Geophysical Research: Atmospheres, 131, e2025JD044219, https://doi.org/10.1029/2025JD044219, 2026.

Smith, C. J., Kramer, R. J., Myhre, G., Alterskjær, K., Collins, W., Sima, A., Boucher, O., Dufresne, J.-L., Nabat, P., Michou, M., Yukimoto, S., Cole, J., Paynter, D., Shiogama, H., O'Connor, F. M., Robertson, E., Wiltshire, A., Andrews, T., Hannay, C., Miller, R., Nazarenko, L., Kirkevåg, A., Olivié, D., Fiedler, S., Lewinschal, A., Mackallah, C., Dix, M., Pincus, R., and Forster, P. M.: Effective radiative forcing and adjustments in CMIP6 models, Atmospheric Chemistry and Physics, 20, 9591–9618, https://doi.org/10.5194/acp-20-9591-2020, 2020.

Soulie, A., Granier, C., Darras, S., Zilbermann, N., Doumbia, T., Guevara, M., Jalkanen, J.-P., Keita, S., Liousse, C., Crippa, M., Guizzardi, D., Hoesly, R., and Smith, S. J.: Global anthropogenic emissions (CAMS-GLOB-ANT) for the Copernicus Atmosphere Monitoring Service simulations of air quality forecasts and reanalyses, Earth System Science Data, 16, 2261–2279, https://doi.org/10.5194/essd-16-2261-2024, 2024.

Su, X., Wei, Y., Wang, L., Zhang, M., Jiang, D., and Feng, L.: Accuracy, stability, and continuity of AVHRR, SeaWiFS, MODIS, and VIIRS deep blue long-term land aerosol retrieval in Asia, Science of The Total Environment, 832, 155048, https://doi.org/10.1016/j.scitotenv.2022.155048, 2022.

Szopa, S., Naik, V., Adhikary, B., Artaxo, P., Berntsen, T., Collins, W. D., Fuzzi, S., Gallardo, L., Kiendler-Scharr, A., Klimont, Z., Liao, H., Unger, N., and Zanis, P.: Short-Lived Climate Forcers, in: Climate Change 2021: The Physical Science Basis. Contribution of Working Group I to the Sixth Assessment Report of the Intergovernmental Panel on Climate Change, edited by: Masson-Delmotte, V., Zhai, P., Pirani, A., Connors, S. L., Péan, C., Berger, S., Caud, N., Chen, Y., Goldfarb, L., Gomis, M. I., Huang, M., Leitzell, K., Lonnoy, E., Matthews, J. B. R., Maycock, T. K., Waterfield, T., Yelekçi, O., Yu, R., and Zhou, B., Cambridge University Press, Cambridge, United Kingdom and New York, NY, USA, 817–922, https://doi.org/10.1017/9781009157896.008, 2021.

Tang, M., Li, K., Liu, Z., Chen, X., Wang, Y., Jin, J., Chen, L., and Liao, H.: Anthropogenic drivers of the accelerated decline in surface NO2 over China during 2015–2022, Environ. Res. Lett., 21, 054003, https://doi.org/10.1088/1748-9326/ae452b, 2026.

Tang, Y., Rumbold, S., Ellis, R., Kelley, D., Mulcahy, J., Sellar, A., Walton, J., and Jones, C.: MOHC UKESM1.0-LL model output prepared for CMIP6 CMIP historical (20250528), https://doi.org/10.22033/ESGF/CMIP6.6113, 2019.

Thornhill, G., Collins, W., Olivié, D., Skeie, R. B., Archibald, A., Bauer, S., Checa-Garcia, R., Fiedler, S., Folberth, G., Gjermundsen, A., Horowitz, L., Lamarque, J.-F., Michou, M., Mulcahy, J., Nabat, P., Naik, V., O'Connor, F. M., Paulot, F., Schulz, M., Scott, C. E., Séférian, R., Smith, C., Takemura, T., Tilmes, S., Tsigaridis, K., and Weber, J.: Climate-driven chemistry and aerosol feedbacks in CMIP6 Earth system models, Atmospheric Chemistry and Physics, 21, 1105–1126, https://doi.org/10.5194/acp-21-1105-2021, 2021.

Tian, C., Yue, X., Zhu, J., Liao, H., Yang, Y., Chen, L., Zhou, X., Lei, Y., Zhou, H., and Cao, Y.: Projections of fire emissions and the consequent impacts on air quality under 1.5 °C and 2 °C global warming, Environmental Pollution, 323, 121311, https://doi.org/10.1016/j.envpol.2023.121311, 2023.

Tian, C., Peng, D., and Yue, X.: Projection of Future Fire Weather in Eurasia by Mid-21st Century, Journal of Geophysical Research: Atmospheres, 130, e2025JD043686, https://doi.org/10.1029/2025JD043686, 2025.

Turnock, S. T., Allen, R. J., Andrews, M., Bauer, S. E., Deushi, M., Emmons, L., Good, P., Horowitz, L., John, J. G., Michou, M., Nabat, P., Naik, V., Neubauer, D., O'Connor, F. M., Olivié, D., Oshima, N., Schulz, M., Sellar, A., Shim, S., Takemura, T., Tilmes, S., Tsigaridis, K., Wu, T., and Zhang, J.: Historical and future changes in air pollutants from CMIP6 models, Atmospheric Chemistry and Physics, 20, 14547–14579, https://doi.org/10.5194/acp-20-14547-2020, 2020.

Turquety, S., Hurtmans, D., Hadji-Lazaro, J., Coheur, P.-F., Clerbaux, C., Josset, D., and Tsamalis, C.: Tracking the emission and transport of pollution from wildfires using the IASI CO retrievals: analysis of the summer 2007 Greek fires, Atmospheric Chemistry and Physics, 9, 4897–4913, https://doi.org/10.5194/acp-9-4897-2009, 2009.

Twomey, S.: Pollution and the planetary albedo, Atmospheric Environment (1967), 8, 1251–1256, https://doi.org/10.1016/0004-6981(74)90004-3, 1974.

Ul-Haq, Z., Tariq, S., and Ali, M.: Tropospheric NO2 Trends over South Asia during the Last Decade (2004–2014) Using OMI Data, Advances in Meteorology, 2015, 959284, https://doi.org/10.1155/2015/959284, 2015.

Van Damme, M., Clarisse, L., Franco, B., Sutton, M. A., Erisman, J. W., Wichink Kruit, R., van Zanten, M., Whitburn, S., Hadji-Lazaro, J., Hurtmans, D., Clerbaux, C., and Coheur, P.-F.: Global, regional and national trends of atmospheric ammonia derived from a decadal (2008–2018) satellite record, Environ. Res. Lett., 16, 055017, https://doi.org/10.1088/1748-9326/abd5e0, 2021.

Van Der Werf, G. R., Randerson, J. T., Giglio, L., van Leeuwen, T. T., Chen, Y., Rogers, B. M., Mu, M., van Marle, M. J. E., Morton, D. C., Collatz, G. J., Yokelson, R. J., and Kasibhatla, P. S.: Global fire emissions estimates during 1997–2016, Earth System Science Data, 9, 697–720, https://doi.org/10.5194/essd-9-697-2017, 2017.

Van Marle, M. J. E., Kloster, S., Magi, B. I., Marlon, J. R., Daniau, A.-L., Field, R. D., Arneth, A., Forrest, M., Hantson, S., Kehrwald, N. M., Knorr, W., Lasslop, G., Li, F., Mangeon, S., Yue, C., Kaiser, J. W., and van der Werf, G. R.: Historic global biomass burning emissions for CMIP6 (BB4CMIP) based on merging satellite observations with proxies and fire models (1750–2015), Geoscientific Model Development, 10, 3329–3357, https://doi.org/10.5194/gmd-10-3329-2017, 2017.

Vohra, K., S., M., Chakraborty, A., Shah, H., As., B., and Pakki, J.: Urgent issues regarding real-time air quality monitoring data in India: Unveiling solutions and implications for policy and health, Atmospheric Environment: X, 25, 100308, https://doi.org/10.1016/j.aeaoa.2024.100308, 2025.

Wang, B., Wen, Z., Que, P., Zhang, T., He, X., Yang, N., Zhong, X., and Xu, Y.: Biodiversity benefits of China's 20-year efforts in forest restoration, Nat Commun, 16, 10724, https://doi.org/10.1038/s41467-025-65751-7, 2025.

Wang, C., Soden, B. J., Yang, W., and Vecchi, G. A.: Compensation Between Cloud Feedback and Aerosol-Cloud Interaction in CMIP6 Models, Geophysical Research Letters, 48, e2020GL091024, https://doi.org/10.1029/2020GL091024, 2021a.

Wang, Z., Zheng, F., Zhang, W., and Wang, S.: Analysis of SO2 Pollution Changes of Beijing-Tianjin-Hebei Region over China Based on OMI Observations from 2006 to 2017, Advances in Meteorology, 2018, 8746068, https://doi.org/10.1155/2018/8746068, 2018.

Wang, Z., Lin, L., Xu, Y., Che, H., Zhang, X., Zhang, H., Dong, W., Wang, C., Gui, K., and Xie, B.: Incorrect Asian aerosols affecting the attribution and projection of regional climate change in CMIP6 models, npj Clim Atmos Sci, 4, 2, https://doi.org/10.1038/s41612-020-00159-2, 2021b.

Wei, J., Li, Z., Peng, Y., and Sun, L.: MODIS Collection 6.1 aerosol optical depth products over land and ocean: validation and comparison, Atmospheric Environment, 201, 428–440, https://doi.org/10.1016/j.atmosenv.2018.12.004, 2019.

Whitburn, S., Clarisse, L., Bouillon, M., Safieddine, S., George, M., Dewitte, S., De Longueville, H., Coheur, P.-F., and Clerbaux, C.: Trends in spectrally resolved outgoing longwave radiation from 10 years of satellite measurements, npj Clim Atmos Sci, 4, 48, https://doi.org/10.1038/s41612-021-00205-7, 2021.

Whitburn, S., Clarisse, L., Crapeau, M., August, T., Hultberg, T., Coheur, P. F., and Clerbaux, C.: A CO_2-independent cloud mask from Infrared Atmospheric Sounding Interferometer (IASI) radiances for climate applications, Atmospheric Measurement Techniques, 15, 6653–6668, https://doi.org/10.5194/amt-15-6653-2022, 2022.

Whitburn, S., Clarisse, L., De Longueville, H., Shine, K. P., Coheur, P. F., Clerbaux, C., and Delcloo, A. W.: Satellite-based estimates of radiative forcing of long-lived halogenated gases from spectral observations, Commun Earth Environ, https://doi.org/10.1038/s43247-026-03691-w, 2026.

Wielicki, B. A., Barkstrom, B. R., Harrison, E. F., Lee, R. B., Smith, G. L., and Cooper, J. E.: Clouds and the Earth's Radiant Energy System (CERES): An Earth Observing System Experiment, Bulletin of the American Meteorological Society, 77, 853–868, https://doi.org/https://doi.org/10.1175/1520-0477(1996)077<0853:CATERE>2.0.CO;2, 1996.

https://doi.org/10.5194/egusphere-2026-4393
Preprint. Discussion started: 17 August 2026

Xie, Y., Zhou, M., Hunt, K. M. R., and Mauzerall, D. L.: Recent PM2.5 air quality improvements in India benefited from meteorological variation, Nat Sustain, 7, 983–993, https://doi.org/10.1038/s41893-024-01366-y, 2024.

Xiong, X. and Barnes, W.: An overview of MODIS radiometric calibration and characterization, Adv. Atmos. Sci., 23, 69–79, https://doi.org/10.1007/s00376-006-0008-3, 2006.

Yang, J. and Huang, X.: The 30m annual land cover dataset and its dynamics in China from 1990 to 2019, Earth System Science Data, 13, 3907–3925, https://doi.org/10.5194/essd-13-3907-2021, 2021.

Yang, Q., Huang, X., and Tang, Q.: Irrigation cooling effect on land surface temperature across China based on satellite observations, Science of The Total Environment, 705, 135984, https://doi.org/10.1016/j.scitotenv.2019.135984, 2020.

Yang, Y., Wang, S., Bai, X., Tan, Q., Li, Q., Wu, L., Tian, S., Hu, Z., Li, C., and Deng, Y.: Factors Affecting Long-Term Trends in Global NDVI, Forests, 10, https://doi.org/10.3390/f10050372, 2019.

Yukimoto, S., Koshiro, T., Kawai, H., Oshima, N., Yoshida, K., Urakawa, S., Tsujino, H., Deushi, M., Tanaka, T., Hosaka, M., Yoshimura, H., Shindo, E., Mizuta, R., Ishii, M., Obata, A., and Adachi, Y.: MRI MRI-ESM2.0 model output prepared for CMIP6 CMIP historical (20250528), https://doi.org/10.22033/ESGF/CMIP6.6842, 2019a.

Yukimoto, S., Koshiro, T., Kawai, H., Oshima, N., Yoshida, K., Urakawa, S., Tsujino, H., Deushi, M., Tanaka, T., Hosaka, M., Yoshimura, H., Shindo, E., Mizuta, R., Ishii, M., Obata, A., and Adachi, Y.: MRI MRI-ESM2.0 model output prepared for CMIP6 ScenarioMIP (20250528), https://doi.org/10.22033/ESGF/CMIP6.638, 2019b.

Yukimoto, S., Kawai, H., Koshiro, T., Oshima, N., Yoshida, K., Urakawa, S., Tsujino, H., Deushi, M., Tanaka, T., Hosaka, M., Yabu, S., Yoshimura, H., Shindo, E., Mizuta, R., Obata, A., Adachi, Y., and Ishii, M.: The Meteorological Research Institute Earth System Model Version 2.0, MRI-ESM2.0: Description and Basic Evaluation of the Physical Component, Journal of the Meteorological Society of Japan. Ser. II, 97, 931–965, https://doi.org/10.2151/jmsj.2019-051, 2019c.

Zhang, X., Liu, J., Han, H., Zhang, Y., Jiang, Z., Wang, H., Meng, L., Li, Y. C., and Liu, Y.: Satellite-Observed Variations and Trends in Carbon Monoxide over Asia and Their Sensitivities to Biomass Burning, Remote Sensing, 12, https://doi.org/10.3390/rs12050830, 2020.

Zhou, M., Xie, Y., Wang, C., Shen, L., and Mauzerall, D. L.: Impacts of current and climate induced changes in atmospheric stagnation on Indian surface PM2.5 pollution, Nat Commun, 15, 7448, https://doi.org/10.1038/s41467-024-51462-y, 2024.